Petroleum Science 23 (2026) 297–316

Contents lists available at ScienceDirect

Petroleum Science

journal homepage: www.keaipublishing.com/en/journals/petroleum-science

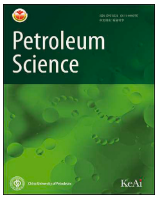

Original Paper

Investigating the effect of the shale bedding structure on hydraulic fracture propagation behavior on the basis of a coupled thermal–hydraulic–mechanical numerical model

Xun Gong [a,b,c,d,e], Zhi-Jun Jin [a,b,*], Xin-Hua Ma [c,d,e], Yu-Yang Liu [c,d,e,**], Yan-Jun Guo [b,f,g], Mei-Zhu Wang [c,d,e]

[a] *Institute of Energy, Peking University, Beijing, 100871, China*
[b] *School of Earth and Space Sciences, Peking University, Beijing, 100871, China*
[c] *Research Institute of Petroleum Exploration and Development (RIPED), PetroChina, Beijing, 100083, China*
[d] *National Energy Shale Gas R&D (Experiment) Center, Langfang, 065007, Hebei, China*
[e] *Key Laboratory of Coal-rock Gas, CNPC, Langfang, 065007, Hebei, China*
[f] *National Experimental Teaching Demonstrating Center of Earth Sciences, Peking University, Beijing, 100871, China*
[g] *National Virtual Simulation Experimental Teaching Center of Earth Sciences, Peking University, Beijing, 100871, China*

ARTICLE INFO

Article history:
Received 29 April 2025
Received in revised form
14 August 2025
Accepted 20 October 2025
Available online 25 October 2025

Edited by Meng-Jiao Zhou

Keywords:
Shale
Bedding
Hydraulic fracturing
Thermal–hydraulic–mechanical coupled
Propagation pattern

ABSTRACT

The interaction process among hydraulic fractures and natural fractures, bedding planes, and other discontinuities during shale fracturing determines the complexity of the fracture network that is formed. However, the current conclusions and understanding of the mechanisms underlying the interaction between hydraulic and natural fractures, as well as their primary controlling factors, fail to meet the requirements of hydraulic fracturing operations, thereby restricting the efficient development of shale gas resources. Therefore, in this study, a coupled thermal–hydraulic–mechanical finite element numerical model that is based on the maximum tensile stress and the Mohr–Coulomb criterion is established, thereby considering rock deformation, fluid flow, and heat transfer. The reliability of this model is validated on the basis of previous research. This model is subsequently employed to simulate the propagation behavior of hydraulic fractures in shale with well-developed bedding. The results indicate that when hydraulic fractures propagate to the bedding, five propagation modes may occur: arrest, diversion, diversion and crossing, crossing and diversion, and direct crossing. These modes are controlled by factors such as the mechanical properties of the shale matrix and bedding, geostress, bedding dip angle, temperature, and fracturing fluid injection rate. During fracture propagation, increases in the elastic modulus ratio between the rock matrix and the bedding, the bedding dip angle, and the temperature are favorable for hydraulic fractures turning along the bedding, whereas increases in the difference in vertical stress and the injection rate are favorable for hydraulic fractures directly crossing the bedding. Second, on the basis of four influencing factors, namely, the shale matrix and bedding elastic modulus ratio, bedding dip angle, difference in vertical stress, and temperature, propagation criteria for hydraulic fractures along the bedding under various combinations of influencing factors are established. The results provide theoretical reference data for the design and optimization of fracturing in shale with well-developed bedding.

1. Introduction

Since the shale gas revolution in the United States, unconventional oil and gas exploration and development have occurred globally. Unconventional oil and gas resources such as shale gas, coalbed methane, and tight sandstone gas have entered a high-

---

* Corresponding author.
** Corresponding author.
E-mail addresses: jinzj1957@pku.edu.cn (Z.-J. Jin), yuyang.liu@pku.edu.cn (Y.-Y. Liu).
Peer review under the responsibility of China University of Petroleum (Beijing).

https://doi.org/10.1016/j.petsci.2025.10.020

speed development stage and have gradually become important supplements to conventional oil and gas resources (Wang et al., 2020; Jarvie et al., 2007; Zou et al., 2012; Miao et al., 2024). Unconventional oil and gas reservoirs such as shale and tight sandstone exhibit low production capacity in their natural state because of their low porosity and permeability and require reservoir stimulation for achieving commercial development (Slatt and O'Brien, 2011; Chalmers et al., 2012; Clarkson et al., 2013; Miao et al., 2023). Hydraulic fracturing, which is a core technology for unconventional oil and gas reservoir stimulation, is important for increasing the storage and production of unconventional oil and gas resources. In the fracturing process, the hydraulic fracture propagation path and its geometry are influenced by factors such as geostress, rock mechanical properties, discontinuities, and construction parameters (Blanton, 1982, 1986; Warpinski and Teufel, 1987; Zou et al., 2021; Hu and Ghassemi, 2021; Zheng et al., 2022). The degree of communication between hydraulic fractures and discontinuities, such as natural fractures, lithological interfaces and bedding, determines the complexity of the generated fracture network, which is also an important indicator of the reservoir stimulation volume (Zheng et al., 2022; Zhang et al., 2021, 2022). The widely developed bedding structure of shale is usually discontinuous. When a hydraulic fracture extends to the bedding, its propagation pattern will become complex under the combined effect of many factors, which leads to difficulty in accurately predicting hydraulic fracture propagation paths and poses an obstacle to fracture design and optimization.

In recent years, scholars have extensively researched the propagation patterns of hydraulic fractures, natural fractures, and other discontinuities, as well as the geometric characteristics of lithological interfaces and bedding structures, through methods such as mine field experiments, indoor hydraulic fracturing model experiments, and numerical simulations and have reached various conclusions and insights. For example, Fu et al. (2020) performed core observations of poststimulation fracturing samples. Their results revealed that parallel fractures are frequently generated during fracturing. On the basis of these findings, they proposed the concept of fracture clusters. Sun et al. (2025) conducted similar postfracturing core studies of the Fuling shale reservoir. Their conclusions agreed with those of Fu et al. (2020). Additionally, they reported that the distance between natural fractures and the wellbore influences the fracture network complexity. Field experiments provide the most reliable data by stimulating fracturing sites during operations. However, existing monitoring techniques cannot accurately capture fracture propagation paths and geometries. Moreover, field tests face limitations because of the limited size of research areas and high costs, which hinders the widespread application of the test results. To reduce expenses and facilitate laboratory-based research, scholars have developed small-scale hydraulic fracturing experiments that involve the use of outcrop samples. This approach enables the indoor and miniaturized simulation of field conditions. Guo et al. (2014) conducted true triaxial hydraulic fracturing experiments involving outcrop shale samples and reported that lower fracturing fluid injection rates and differences in principal stress were conducive to the formation of complex fracture networks. Subsequently, Xu et al. (2015) conducted hydraulic fracturing experiments of shale with well-developed bedding and reported that the smaller the difference in principal stress is, the more likely the turning of hydraulic fractures along the bedding is. These results validate the findings of Guo et al. (2014). By performing hydraulic fracturing experiments of outcrop shale samples, Tan et al. (2017, 2018) determined that in addition to geostress, the strength of bedding cementation is an important factor that influences the propagation pattern of hydraulic fractures. Zhang et al. (2023a) conducted hydraulic fracturing experiments involving outcrop shale and reported that termination, diversion, direct crossing, and composite propagation occurred mainly when hydraulic fractures extended to the bedding, and these conclusions have been confirmed by numerous scholars (Cong et al., 2024; Warpinski and Teufel, 1987; Tan et al., 2017, 2018; Wu et al., 2022a; Hou et al., 2018; Lu et al., 2023; Jiang et al., 2023; Zhang et al., 2021). By conducting hydraulic fracturing experiments of shale samples, Liu et al. (2021) determined that the rock rupture pressure was negatively correlated with the stratigraphic dip and borehole size. Zhao et al. (2022) conducted hydraulic fracturing experiments of shale and reported that the pumping pressure and vertical stress notably affected the propagation pattern of hydraulic fractures and that the rupture pressure increased with increasing vertical stress. Wu et al. (2022a) simulated the propagation behavior of hydraulic fractures in reservoirs containing bedding by conducting true triaxial hydraulic fracturing experiments of shale. It has been indicated that the bedding structure is the main factor influencing interseam interference and that it also restricts the propagation height of hydraulic fractures. The above scholars conducted hydraulic fracturing experiments of shale samples to analyze the propagation morphology of hydraulic fractures in the fracturing process and its influencing mechanisms and reported that the propagation morphology of hydraulic fractures and its influencing factors are comprehensively influenced by numerous geological and engineering factors. Indoor hydraulic fracturing experiments aim to simulate field experiments on a smaller scale, and the results obtained via this method are highly reliable; thus, it is a commonly employed method in hydraulic fracturing research. However, hydraulic fracturing experiments are relatively costly and involve certain risks. In addition, the results of these experiments are influenced by size effects, which suggests that the results obtained via this method do not fully conform with those obtained at fracturing sites in the field, thus limiting the widespread application of this method.

With the development of computer technology, numerical methods such as the finite element method (FEM), extended finite element method (XFEM), boundary element method (BEM), discrete element method (DEM), and phase field method (PFM) have been introduced into hydraulic fracturing research and have gradually yielded important methods (Shentu et al., 2024; Ju et al., 2019; Qin and Yang, 2023; Zhou et al., 2018, 2020; Ouchi et al., 2017; Lecampion et al., 2018; Cundall and Strack, 2008; Chen et al., 2021; Gong et al., 2025a). Liao et al. (2024) employed a numerical model that was established via the FEM to simulate the vertical propagation of hydraulic fractures during fracturing. The results revealed that differences in vertical stress and rock interfacial strength control the propagation pattern of hydraulic fractures at rock interfaces. Zhang et al. (2024) simulated the interaction process between hydraulic fractures and shale bedding by applying a numerical model that was established via the XFEM and reported that factors such as differences in the mechanical properties of the rock matrix and bedding and geostress notably influence the propagation of hydraulic fractures. Via the use of a numerical model established through the DEM, Zheng et al. (2022) analyzed the effects of the fracturing fluid viscosity and injection rate on the propagation behavior of hydraulic fractures at the bedding. High viscosity and a high injection rate are conducive to hydraulic fractures directly crossing the bedding. Li and Wu. (2022a) investigated the influence of the bedding interface on the geometry and width distribution of hydraulic fractures via a numerical model that was established through the displacement discontinuity method (DDM). The results revealed that the lateral extension of hydraulic fractures is beneficial and that the interface spacing and shear toughness notably influence the geometry and width of hydraulic fractures. Zeng et al. (2023a) simulated the extension behavior of hydraulic fractures at a lithological interface through a numerical model that was established with the PFM and reported that factors such as the mechanical properties of the rocks on both sides of the lithological interface, the injection pressure, and the geostress greatly influence the extension behavior of hydraulic fractures at the interface. This conclusion was also confirmed by Gong et al. (2025a). In addition to using a single numerical method, scholars have combined multiple numerical methods to analyze the propagation behaviors of hydraulic fractures during fracturing. Gong et al. (2025b) considered the widespread development of shale bedding structures and combined the advantages of the PFM and the cohesive element method to establish a thermal–hydraulic–solid coupled numerical model for simulating the propagation behavior of hydraulic fractures in bedding structures. The results revealed that bedding structures, which are weak surfaces, are the primary cause of the complex and variable propagation paths of hydraulic fractures. Ma et al. (2023) employed a numerical model that was developed via the XFEM and the cohesive zone method (CZM) and reported that hydraulic fractures can easily cross the interface between hard and soft rock layers. Zeng et al. (2023b) applied a numerical model that was established via the FEM and the CZM to simulate the interaction process between hydraulic fractures and bedding planes. The results demonstrated that an increase in the difference in vertical stress is conducive to hydraulic fractures directly crossing the interface. Wu et al. (2022b) simulated the propagation behavior of a hydraulic fracture at the interface with a model that was developed via the FEM in combination with the DEM and reported that the degree of slip at the interface determines whether the hydraulic fracture passes through the interface. The different numerical methods exhibit distinct advantages and shortcomings. Therefore, on the basis of the characteristics of the research subject, considering the advantages and disadvantages of various numerical methods and selecting the most appropriate option are important. Compared with other numerical methods, the FEM, which was the first research method to be introduced into hydraulic fracturing, offers the advantages of a wide range of applications and has been applied in abundant research cases; therefore, the accuracy of the results obtained via this method is high. The propagation behavior of hydraulic fractures along the bedding in shale formations with well-developed laminations is complex and variable, and the underlying mechanisms remain incompletely understood. Current knowledge regarding the interactions between hydraulic fractures and natural fractures, lithological interfaces, and other discontinuities—particularly bedding—remains insufficient to meet the practical demands of field-scale hydraulic fracturing operations. To address this gap, a coupled thermal−hydraulic−mechanical finite element numerical model with laboratory-scale hydraulic fracturing dimensions is developed by integrating theoretical frameworks from rock mechanics, damage mechanics, fracture mechanics, elasticity theory, and porous media mechanics. The model relies on the maximum tensile stress criterion for tensile−-compressive damage and the Mohr−Coulomb criterion for shear damage, fluid flow is governed by Darcy's law, and heat exchange between the fracturing fluid and reservoir rock is characterized by Fourier's law of heat conduction. Additionally, rock heterogeneity is accounted for via the Weibull distribution. By incorporating temperature variations, rock deformation, fluid flow dynamics, and inherent rock heterogeneity, the model effectively captures subsurface hydraulic fracturing processes. Through numerical simulations, the propagation behavior of hydraulic fractures along shale bedding is investigated, and the controlling mechanisms are analyzed, thereby elucidating the influence of the bedding structure on fracture propagation. The findings provide theoretical insights for optimizing laboratory-scale hydraulic fracturing experiments and field-scale fracturing design.

The remainder of this article is organized as follows: Section 2 offers a description of the governing equations that are associated with the mathematical model. Section 3 provides an examination of the numerical solution process and the solution method. Section 4 presents a verification of the reliability of the model. Section 5 provides an analysis of the propagation pattern of hydraulic fractures in bedding and its influencing factors. Section 6 offers an exploration of the propagation patterns of hydraulic fractures in reservoirs with widely developed bedding and its influencing factors. Finally, Section 7 concludes the article.

2. Mathematical model

The basic assumptions of the numerical model are as follows (Lei et al., 2021; Zhang et al., 2023b): (1) The established numerical model is a dual-media model that comprises a rock matrix and fractures. (2) Numerous bedding structures are developed in shale, which can become bedding fractures under unconfined conditions, and the mechanical strength of bedding structures is assumed to be lower than that of the rock matrix, whereas the porosity and permeability are assumed to be greater than those of the rock matrix. (3) The fluid flow complies with Darcy's law, and there is no chemical reaction with the rock. (4) The shale meets the assumption of small deformation, and there is no phase change throughout the simulation process.

2.1. Rock deformation

The mechanical equilibrium equations for rocks during quasi-static loading are as follows:

$$\nabla \cdot \sigma_{ij,j} + F_i = 0 \tag{1}$$

where σ_{ij} denotes the total stress tensor and F_i denotes the body force per unit volume of rock, Pa/m.

Under the assumption that shale is a linear elastic porous medium and considering both the pore fluid pressure and thermal stress effects, the constitutive equation can be expressed as follows:

$$\sigma_{ij} = 2G\varepsilon_{ij} + \frac{2G\nu}{1-2\nu}\delta_{ij}\varepsilon_{kk} - \alpha p\delta_{ij} - \frac{2G(1+\upsilon)\alpha_{\mathrm{m}}^{T}}{3(1-2\upsilon)}T\delta_{ij} \tag{2}$$

where G denotes the shear modulus, Pa; p denotes the pore pressure, Pa; α denotes the Biot coefficient (α_{m} and α_{b} denote the ratios of the rock matrix and fractures, respectively), which varies with increasing damage degree of the rock; ν denotes the dimensionless Poisson's ratio; δ_{ij} denotes the Kronecker number; T denotes the temperature variable; and α_{m}^{T} denotes the thermal expansion coefficient.

On the basis of the conservation of momentum and considering the effects of the pore fluid pressure and thermal stress, the following stress balance equation can be obtained:

$$Gu_{i,jj} + \frac{G}{1-2\nu}u_{j,ji} - \alpha p_{,i} - \frac{2G(1+\upsilon)\alpha_{\mathrm{m}}^{T}}{3(1-2\upsilon)}(T-T_0) + F_i = 0 \tag{3}$$

where T and T_0 denote the real-time and initial temperatures, respectively, K.

2.2. Fluid flow in porous media

Considering shale as a porous medium throughout the fracturing process and accounting for the porous elasticity effect, the mass conservation equation for fluid flow is as follows:

$$\rho_{\mathrm{f}} S \frac{\partial p}{\partial t} - \nabla \cdot \left(\rho_{\mathrm{f}} \vec{v}\right) = Q - \rho_{\mathrm{f}} \alpha \frac{\partial \varepsilon_{\mathrm{vol}}}{\partial t} \tag{4}$$

where ρ_{f} denotes the fluid density, kg/m^3; S denotes the storage coefficient of the porous medium (S_{m} and S_{b} denote the storage coefficients of the matrix and fractures, respectively); $\vec{v}$ denotes the fluid velocity vector; Q denotes the sink term (Q_{m} and Q_{b} denote the source−sink terms for the rock matrix and fractures, respectively); and $\varepsilon_{\mathrm{vol}}$ denotes the volumetric strain.

Ignoring the effects of gravity, Darcy's velocity can be calculated as follows:

$$\vec{v} = -\frac{K}{\mu} \nabla p \tag{5}$$

where K denotes the permeability of the porous medium (K_{m} and K_{b} denote the matrix and fracture permeabilities, respectively), m^2, and μ denotes the fluid dynamic viscosity, Pa·s.

The water storage coefficient of the porous medium can be expressed as follows:

$$S = \varphi c_{\mathrm{f}} + \frac{(\alpha - \varphi)(1 - \alpha)}{K_{\mathrm{v}}} \tag{6}$$

where c_{f} denotes the fluid compression coefficient, K_{v} denotes the bulk modulus of the porous medium (K_{vm} and K_{vb} denote the rock matrix and fracture bulk moduli, respectively), and φ denotes the porosity (φ_{m} and φ_{b} denote the rock matrix and fracture porosities, respectively).

Second, for the rock matrix, the porosity can be obtained as follows:

$$\varphi_{\mathrm{m}} = \varphi_{\mathrm{mr}} + (\varphi_{\mathrm{m0}} - \varphi_{\mathrm{mr}}) \exp\left(-\xi \sigma_{\mathrm{ef}}\right) \tag{7}$$

where φ_{m0} and φ_{mr} denote the initial and residual porosities of the rock matrix, respectively, and ξ denotes the rock matrix pore–stress correlation coefficient, which can be calculated as follows (Lei et al., 2021; Wu et al., 2023):

$$\xi = \begin{cases} \dfrac{C_{\mathrm{m}}}{\varphi_{\mathrm{m0}} - \varphi_{\mathrm{mr}}}, & D = 0 \\ \dfrac{1}{[K_{\mathrm{n}}(b_0 - b_{\mathrm{r}})]}, & D > 0 \end{cases} \tag{8}$$

where $C_{\mathrm{m}} = \frac{3(1-2\nu)}{E}$ is the rock matrix drainage compressibility; K_{n} denotes the normal stiffness, the details of which can be found in the literature (Lei et al. (2021)); b_0 and b_{r} denote the initial and residual apertures of the fractures, respectively; and D denotes the damage factor, which indicates the degree of rock deterioration.

In addition, σ_{ef} denotes the average effective stress, which can be calculated as follows:

$$\sigma_{\mathrm{ef}} = \frac{(\sigma_1 + \sigma_2 + \sigma_3)}{3} - \alpha p \tag{9}$$

where σ_1, σ_2 and σ_3 denote the three-way principal stresses, Pa.

The rock matrix permeability can be calculated as follows:

$$K_{\mathrm{m}} = K_{\mathrm{m0}} \left(\frac{\varphi_{\mathrm{m}}}{\varphi_{\mathrm{m0}}}\right)^3 \exp(\varsigma D) \tag{10}$$

where K_{m0} denotes the initial permeability of the rock matrix, D denotes the damage evolution parameter, and ς denotes the permeability−stress correlation coefficient of the rock matrix, with a value of 5 adopted in this study (Zhang et al., 2023b).

For discontinuities such as natural fractures and bedding in rocks, the porosity can be calculated as follows:

$$\varphi_{\mathrm{b}} = \varphi_{\mathrm{br}} + (\varphi_{\mathrm{b0}} - \varphi_{\mathrm{br}}) \exp\left(-\zeta \sigma_{\mathrm{ef}}\right) \tag{11}$$

where φ_{b0} and φ_{br} denote the initial and residual porosities of the fracture, respectively, and ζ denotes the fracture porosity−stress correlation coefficient, with a value of 5 × 10^{-8} chosen in this study, Pa^{-1} (Zhang et al., 2023b).

Moreover, the permeability of discontinuities such as natural fractures and bedding can be calculated as follows:

$$K_{\mathrm{b}} = K_{\mathrm{b0}} \exp\left(a \sigma_{\mathrm{n}}'\right) \tag{12}$$

where K_{b0} denotes the initial permeability of the fracture, a denotes the normalization constant related to the deformation of the fracture (Zhang et al., 2019), and σ_{n}' denotes the effective normal stress that acts on the fracture surface, which can be expressed as follows:

$$\sigma_{\mathrm{n}}' = \sigma_{\mathrm{n}} - \alpha p \tag{13}$$

where σ_{n} denotes the normal stress that acts on the fracture surface.

2.3. Heat transfer equation

In the fracturing process, under the assumption that the shale and fluid occur in local thermal equilibrium and considering heat convection and heat conduction, the heat transfer equation is expressed as follows:

$$\left(\rho C_{\mathrm{p}}\right)_{\mathrm{eq}} \frac{\partial T}{\partial t} + \rho_{\mathrm{f}} C_{\mathrm{pf}} \vec{v} \cdot \nabla T = \nabla \cdot \left(\lambda_{\mathrm{eq}} \nabla T\right) + Q_0 \tag{14}$$

where Q_0 denotes the heat source and the specific equations for the remaining parameters are as follows:

$$\left(\rho C_{\mathrm{p}}\right)_{\mathrm{eq}} = \varphi_{\mathrm{m}} \rho_{\mathrm{f}} C_{\mathrm{pf}} + (1 - \varphi_{\mathrm{m}}) \rho_{\mathrm{m}} C_{\mathrm{pm}} \tag{15}$$

$$\lambda_{\mathrm{eq}} \nabla T = \varphi_{\mathrm{m}} \lambda_{\mathrm{f}} + (1 - \varphi_{\mathrm{m}}) \lambda_{\mathrm{m}} \tag{16}$$

where C_{pm} and C_{pf} denote the constant-pressure heat capacities of the reservoir rock and fluid, respectively, and λ_{m} and λ_{f} denote the heat conductions of the reservoir rock and fluid, respectively.

The change in heat transfer through the rock during fracturing can be expressed as follows:

$$\lambda = \lambda_0 \exp(D \alpha_{\mathrm{T}}) \tag{17}$$

where λ denotes the thermal conductivity (λ_{m} and λ_{b} denote the reservoir rock and fracture thermal conductivities, respectively), λ_0 denotes the initial thermal conductivity (λ_{m0} and λ_{b0} denote the reservoir rock and fracture initial thermal conductivities, respectively), and α_{T} denotes the coefficient of the thermal conductivity (α_{Tm} and α_{Tb} are the coefficients for the reservoir rock and fractures, respectively), which varies for different values of the rock matrix and fracture properties (Zhang et al., 2023b).

2.4. Damage evolution equation

Shale is generally considered brittle rock. Therefore, in this research, the maximum tensile stress criterion and the Mohr−-Coulomb criterion are used as rock damage criteria (Zhu and Tang, 2002; Cheng et al., 2023; Wu et al., 2023). First, we determine whether F_1 is greater than or equal to 0, and then we determine whether F_2 is greater than or equal to 0. As long as one of these variables is greater than or equal to 0, rock rupture occurs, which can be expressed as follows:

$$\begin{cases} F_1 = \sigma_1 - f_\mathrm{T} \\ F_2 = -\sigma_3 - f_\mathrm{C} + \dfrac{1+\sin\theta}{1-\sin\theta}\sigma_1 \end{cases} \tag{18}$$

where F_1 and F_2 denote the queue functions of tensile and shear damage, respectively, Pa; σ_1 and σ_3 denote the maximum and minimum principal stresses, respectively, Pa; f_T and f_C denote the tensile and compressive strengths, respectively, of the rock, Pa; and θ denotes the angle of internal friction, ° (θ_m and θ_b denote the angles of internal friction of the rock matrix and the fracture, respectively).

In the rock damage evolution process, the damage factor D is used to indicate the degree of damage to the rock, where a value of 0 indicates that the rock is intact, whereas a value of 1 indicates that the rock is completely damaged; the expression is as follows:

$$D = \begin{cases} 1,\ F_1 < 0,\ F_2 < 0 \\ 1 - \left|\dfrac{\varepsilon_\mathrm{t}}{\varepsilon_1}\right|^2, F_1 = 0,\ \mathrm{d}F_1 > 0 \\ 1 - \left|\dfrac{\varepsilon_\mathrm{c}}{\varepsilon_3}\right|^2,\ F_2 = 0,\ \mathrm{d}F_2 > 0 \end{cases} \tag{19}$$

where ε_t and ε_c denote the tensile and shear strains, respectively, and ε_1 and ε_3 denote the maximum and minimum principal strains, respectively.

The process of rock damage during fracturing is irreversible. Therefore, the mechanical properties of the rock gradually deteriorate with increasing degree of damage, and when the damage factor D equals 1, the rock is completely damaged. In the damage process, the change in the rock elastic modulus can be expressed as follows:

$$E = E_0(1-D) \tag{20}$$

where E_0 denotes the initial modulus of elasticity of the rock.

In addition, in the fracturing process, fresh water is used as the fracturing fluid, the degree of which decreases with increasing temperature, and COMSOL's equation is used to calculate this parameter as follows:

$$\rho_\mathrm{f} = 545.28 + 5.749816T - 0.0157244T^2 + 1.264375E^{-5}T^3 \tag{21}$$

In the fracturing process, the viscosity of the fracturing fluid decreases gradually with increasing temperature, and COMSOL's equation is used to calculate the viscosity as follows:

$$\mu = \exp\left(3.48378315E^{-9}T^4 - 5.27092524E^{-6}T^3 + 3.02511035E^{-3}T^2 - 7.90657912E^{-1}T + 7.19634916E\right) \tag{22}$$

2.5. Rock heterogeneity

Shale comprises mainly of quartz, feldspar, dolomite, pyrite and other minerals. Under high temperature and pressure, different minerals exhibit different mechanical properties, which leads to high heterogeneity in shale. Research has shown that the heterogeneity in shale notably influences the extension of hydraulic fractures. Therefore, in this study, the Weibull distribution is used to characterize the heterogeneity caused by differences in the shale mineral composition. The lower the heterogeneity coefficient value is, the greater the heterogeneity in the rock sample. On this basis, and with reference to previous studies, the heterogeneity coefficient is set to 10 to characterize the heterogeneity in the mechanical properties of shale (Guo et al., 2021; Wu et al., 2023; Zhang et al., 2023b), such as the elastic modulus and strength. The specific expression is as follows:

$$f(\chi) = \frac{b}{\chi_0}\left(\frac{\chi}{\chi_0}\right)^{b-1} \exp\left(-\frac{\chi}{\chi_0}\right)^b \tag{23}$$

where χ is a mechanical parameter; χ_0 is a scale parameter of the rock sample cell, which is related to the average shear rupture strength of all the cells; and b is the heterogeneity coefficient. The lower its value is, the higher the heterogeneity in the rock (Guo et al., 2021; Zhang et al., 2023b).

3. Numerical solution

The fracturing process involves coupled thermal–fluid–mechanical–damage processes that are highly nonlinear in both the temporal and spatial domains, thus rendering the solution process difficult. Commercial software COMSOL Multiphysics relies on finite elements for obtaining the solution and provides a series of solvers and external interfaces for MATLAB, which can effectively address the computation of the combined nonlinear equations. Therefore, considering the difference in mechanical parameters between the rock matrix and bedding, in this research, MATLAB software, in combination with the Weibull distribution, is first used to characterize heterogeneous rock mechanical parameters such as the elastic modulus, tensile strength and compressive strength in the model domain, and the strength of the bedding must be lower than that of the rock matrix. On the basis of the maximum tensile stress criterion and the Mohr–Coulomb criterion, the rock damage criterion is defined in the model component, which serves as the damage criterion for the subsequent calculation process. Second, the rock deformation equations, fluid flow equations, and heat transfer equations that are involved in the model are first initialized via the steady-state solver, and the transient solver is then applied for simultaneous solving. The specific settings of the transient solver are as follows: the time domain is discretized via the implicit solution method, the relative tolerance is set to 0.001, the time step is set to 1, and the full-coupling algorithm is selected for solving. The specific solution steps are as follows (see Fig. 1):

(1) Heterogeneous mechanical parameters such as the elastic modulus, compressive strength, and tensile strength at the model scale are generated with MATLAB.

(2) In COMSOL Multiphysics, the Solid Mechanics, Darcy's Law, and Heat Transfer in Porous Media modules are selected, a geometrical model is established, the model parameters are input, and the model boundary conditions and initial conditions are defined. Moreover, the tensile and compressive damage criteria for rocks are defined under the definition

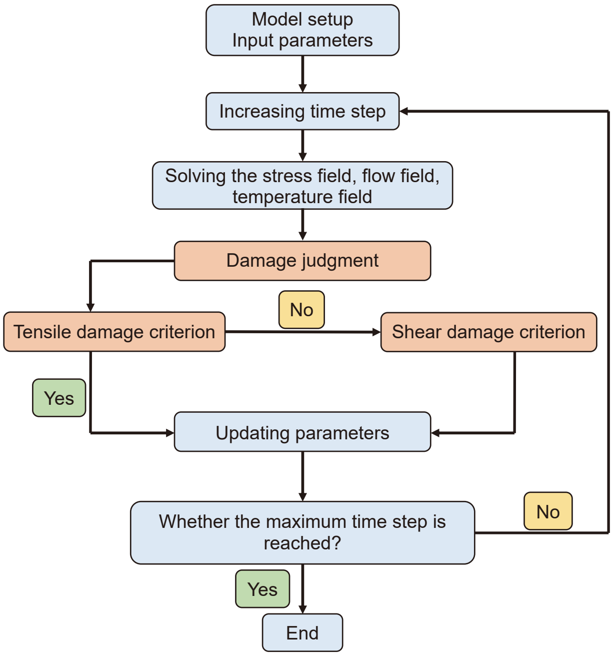

Fig. 1. Flowchart of the model solution process.

subnode of the component, which serve as damage criteria in the subsequent calculation process.

(3) The model is first solved in the steady state. In one time step, the steady-state solver is chosen to compute the rock deformation, fluid flow, and heat transfer to initialize the model.
(4) Then, a fully coupled algorithm is selected to solve the model in the framework of the transient solver. The tensile and shear damage criteria are employed to assess the nodal cells. The tensile stress is evaluated first, and the shear stress is then assessed if the damage conditions are not satisfied. The parameters are processed according to the results
(5) The time step is increased sequentially, and the above steps are repeated until the maximum time step is reached.

4. Model validation

In this section, the reliability of the obtained model results is verified. The model is validated on the basis of hydraulic fracturing experimental results and numerical simulation results.

4.1. Comparison with experimental results

Hydraulic fracturing experiments are typically conducted to study the mechanism of hydraulic fracture propagation and are often employed to validate hydraulic fracturing numerical simulation results. On the basis of recent experimental studies on the hydraulic fracturing of hard rocks, such as shale, tight sandstone, and hot dry rock, in this study, a coupled thermal–hydraulic–mechanical numerical model is first applied to simulate previous experimental results. The simulation results are then compared with the experimental results to verify the model reliability. Zhou et al. (2020a) analyzed the propagation patterns of hydraulic fractures and their impact mechanisms under thermal–hydraulic–mechanical coupling by conducting true triaxial hydraulic fracturing experiments of hot dry rocks. Therefore, in this study, a two-dimensional model, with a size of 300 × 300 mm, is established according to the experimental requirements of Zhou et al. (2020a), and the boundary conditions, rock mechanical parameters and construction parameters of the model are defined by following the experimental requirements of Zhou et al. (2020a) as much as possible. The simulation results are shown in Fig. 2. Notably, the hydraulic fracture initiates from the wellbore and then extends along the direction of the maximum horizontal principal stress, which is consistent with the experimental results of Zhou et al. (2020a), thereby demonstrating that the established coupled thermal–hydraulic–mechanical numerical model can realistically simulate the hydraulic fracturing process of hard rocks such as hot dry rocks, shale, and tight sandstone. Moreover, various degrees of bending occur in the fracture extension process, which results in the numerical simulation results and experimental results failing to match completely, which is attributed to the heterogeneity in the rock as well as the incomplete agreement of the simulation parameters.

4.2. Interaction of hydraulic fractures with natural fractures

Reservoir rocks develop discontinuities such as faults, joints, natural fractures, and bedding, which notably influence the propagation patterns of hydraulic fractures and their paths in the fracturing process. Scholars have investigated the interaction mechanism between hydraulic and natural fractures in depth and have concluded that when hydraulic fractures approach natural fractures, they may turn, terminate or pass through the natural fractures directly. The resultant situation is controlled by geological factors such as geostress, rock mechanical properties, natural fractures and engineering factors such as the properties of the

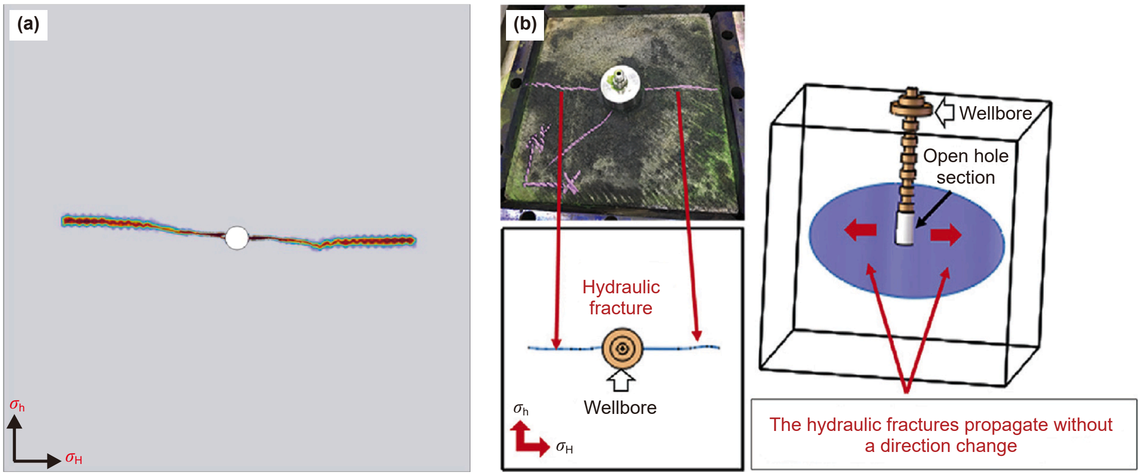

Fig. 2. Results of physical modeling experiments and numerical simulations (Zhou et al., 2020a). (**a**) Numerical simulation, (**b**) hydraulic fracturing tests.

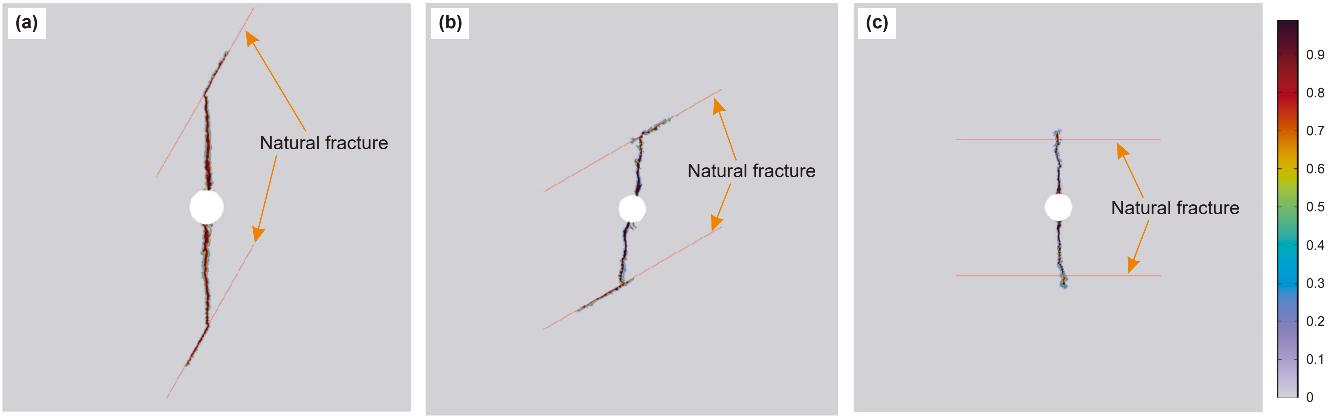

Fig. 3. Numerical simulation results for a principal stress difference of 4 MPa. (**a**) Approach angle of 30° and turning, (**b**) approach angle of 60° and turning, and (**c**) approach angle of 90° and direct crossing.

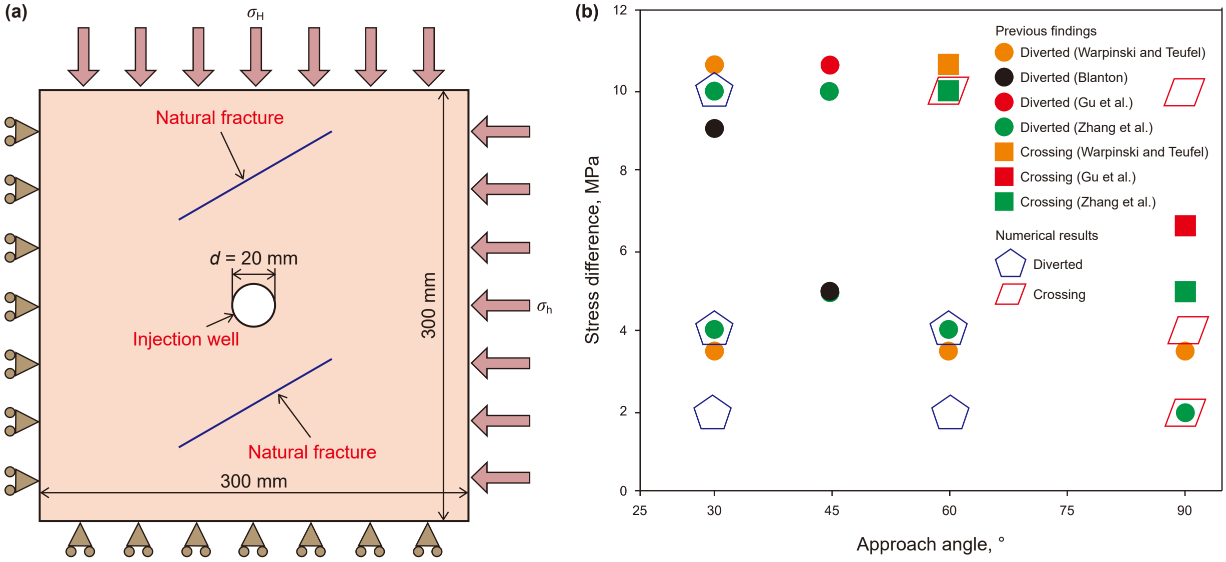

Fig. 4. Geometric boundary and simulation results (Zhang et al., 2023b; Blanton, 1986; Warpinski and Teufel, 1987; Gu et al., 2012). (**a**) Geometric boundary of the model and (**b**) experimental and simulation results.

fracturing fluid and proppant (Zhou et al., 2022; Zhao et al., 2022; Li and Wu, 2022b; Gong et al., 2024; Sarmadi et al., 2024). Therefore, in this study, we verify the model reliability by comparing the numerical simulation results with previous numerical simulation results and fracturing experimental results and by analyzing the interaction behavior of hydraulic fractures with natural fractures under various combinations of geostresses and angles of approximation (intersection angles between hydraulic and natural fractures). The details are as follows: first, a 300 × 300 mm two-dimensional coupled thermal–hydraulic–mechanical–damage model is established according to the results of previous studies. At the center of the model, a 20-mm-diameter borehole is established, and there are natural fractures of an identical nature with a length of 150 mm on both sides of the model. The left and lower sides of the model are fixed surfaces, and the upper and right sides are subjected to the maximum horizontal stress and the minimum horizontal stress, respectively (Fig. 4(a)). The fracturing fluid is injected at a constant rate during the simulation, and the applied principal stress differences are 2, 4 and 10 MPa; subsequently, the interaction behaviors between the hydraulic and natural fractures are simulated at approximation angles of 30°, 60°, and 90°. Additionally, the selection of parameters such as the porosity, permeability and rock mechanical properties throughout the simulation process is as consistent as possible with that in previous studies to reduce the influence of parameter differences on the simulation results. The simulation results are shown in Fig. 3(a) and (b). When the principal stress differences are 2 and 4 MPa and the approximation angles are 30° and 60°, respectively, the hydraulic fracture turns along the natural fracture when it reaches the latter. When the principal stress difference is 2 and 4 MPa and the approximation angle is increased to 90°, the hydraulic fracture directly crosses the natural fracture when it approaches the latter (Figs. 3(c) and 4(b)). When the principal stress difference increases to 10 MPa and the angle of approximation is 30°, the hydraulic fracture extends to the natural fracture and turns along it; as the angle of approximation increases to 60° and 90°, the hydraulic fracture passes directly through the natural fracture as it approaches the latter (Fig. 4(b)). The other parameters are maintained constant, and with increasing approach angle and difference in principal stress, the behavior of the hydraulic fracture gradually changes from turning along the natural fracture to crossing its directly when it extends to the latter. In other words, increases in the difference in principal stress and the approximation angle are favorable for the hydraulic fracture to directly pass through the natural fracture. This conclusion is consistent with previous conclusions, which verifies the reliability of the model. Moreover, minor differences are observed between the hydraulic fracture extension morphology and the previous results, which can be attributed to the incomplete matching of the selected parameter values and the heterogeneity in the rock.

5. Analysis of the propagation patterns of hydraulic fractures in formations with bedding and their influencing factors

Scholars have numerically studied the influence of the shale bedding structure on the extension behavior of hydraulic fractures and have reached certain conclusions. On the basis of the established coupling thermal–fluid–mechanical–damage model, the extension behavior of hydraulic fractures in formations with bedding is simulated in this study, and the mechanism underlying the influence of the shale bedding structure on hydraulic fracture extension is investigated. The geometric boundaries and mechanical parameters of the model are selected on the basis of the results of the hydraulic fracturing experiments and rock mechanics experiments. Specifically, the side length of the model is 300 mm, the borehole (with a radius of 10 mm) is located at the center of the model, the fracturing fluid is injected mainly along the wellbore, and the injection rate is maintained constant (Fig. 5(a)). Moreover, straight lines are inserted every 100 mm along the longitudinal direction to indicate the bedding structure (Fig. 5(a)). As shown in Fig. 5, the borehole is used as the center of the model, with one bedding above and below it, whose distance from the center of the borehole is 50 mm; thus, the rock matrix is divided into three parts (Fig. 5(a)). The left and lower boundaries of the model are defined as fixed surfaces, with 14 MPa vertical stress applied to the upper boundary and 10 MPa minimum horizontal stress applied to the right boundary, and the initial pore pressure remains constant (Fig. 5(a)).

Second, the established model is meshed and discretized. In this research, free triangular grid cells are used to discretize the entire model domain. The grid cell size of both the bedding and borehole boundaries is set to 0.5 mm; the minimum grid cell size of the model domain is 0.5 mm, and the maximum is 3 mm, with a cell growth rate of 1.05 (Fig. 5(b)). This ensures that the model simulation results are only minimally affected by the grid division, which in turn increases the accuracy of the simulation results.

Shale bedding is closed under subsurface *in situ* conditions because of the surrounding pressure, but in the unconfined state, bedding cracks easily develop. Therefore, scholars generally regard shale bedding as a weak plane whose mechanical parameters, such as the modulus of elasticity and strength, are much lower than those of the rock matrix, whereas its porosity and permeability are greater than those of the rock matrix. Therefore, to capture the actual geological conditions as much as possible, different parameter values are set for the shale bedding and rock matrix throughout the simulation process. The mechanical strength parameter of the rock matrix is greater than that of the bedding, whereas the porosity and permeability are lower than those of the bedding. In addition, the 300 mm square shale samples used in the hydraulic fracturing experiments possess the same material source and depositional environment, so the elastic modulus, mechanical strength, porosity, and permeability of the shale matrix are identical, and there are large differences only in the bedding structure. This study also follows these guidelines for the selection of rock matrix and bedding parameters. The selected model parameters are listed in Table 1. The rock mechanical parameters are derived mainly from experimental test results, whereas the remaining parameters are derived from previous results (Yaghoubi, 2019; Zhang et al., 2023; Yin et al., 2023; Lei et al., 2024), thereby ensuring that the model parameters are as close to reality as possible.

5.1. Hydraulic fracture propagation pattern in bedding

Shale features massive bedding structures with high heterogeneity and anisotropy, which poses a serious obstacle to the accurate prediction of hydraulic fracture extension paths. Deep underground shale is subjected to high temperatures and high pressures, which results in closed bedding; when shale is removed, it becomes unconfined, and bedding fractures are developed. Therefore, we can regard the bedding structure that is developed in shale as a type of weak plane, and its properties, such as elastic modulus and mechanical strength, are much weaker than those of the rock matrix. Bedding fractures, which are a type

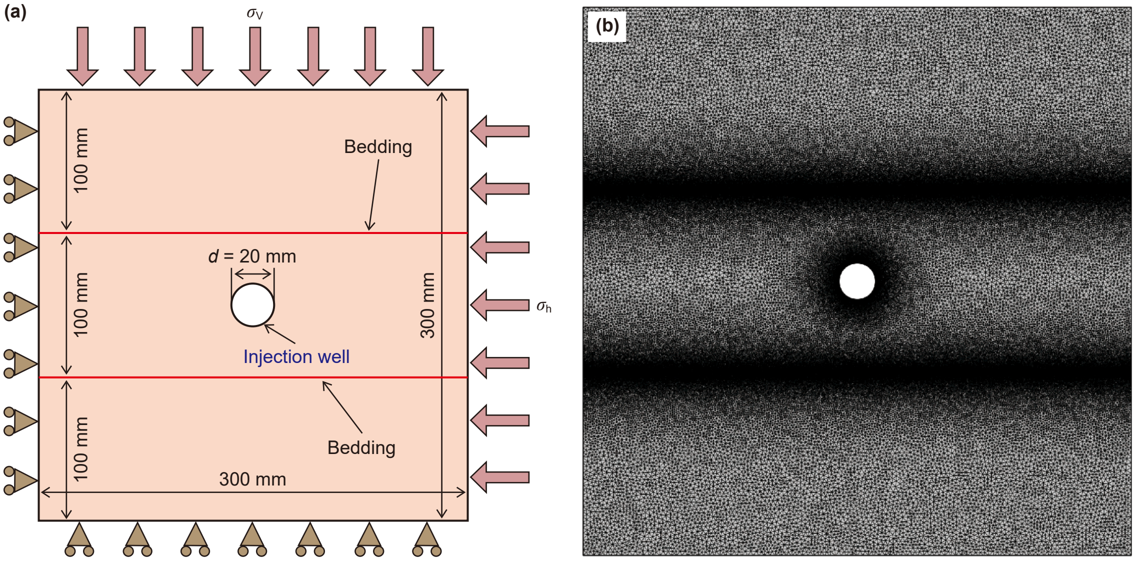

Fig. 5. Model geometric boundary and meshing. (**a**) Model geometric boundary and (**b**) mesh division.

Table 1
Selected model parameters (Yaghoubi, 2019; Zhang et al., 2023; Yin et al., 2023; Lei et al., 2024; Zhou et al., 2020b).

Parameter	Magnitude	Parameter	Magnitude
Rock matrix		Bedding	
Elastic modulus (E_{m}), GPa	20	Elastic modulus (E_{b}), GPa	5
Poisson's ratio (ν_{m})	0.2	Poisson's ratio (ν_{b})	0.25
Density (ρ_{m}), kg/m^3	2700	Density (ρ_{b}), kg/m^3	2000
Compressive strength (f_{Cm}), MPa	120	Compressive strength (f_{Cb}), MPa	30
Tensile strength (f_{Tm}), MPa	8	Tensile strength (f_{Tb}), MPa	2
Thermal expansion coefficient (λ_{m}), K^{-1}	2×10^{-6}	Thermal expansion coefficient (λ_{b}), K^{-1}	4×10^{-6}
Heat capacity (C_{pm}), J/(kg·K)	950	Heat capacity (C_{pb}), J/(kg·K)	850
Initial thermal conductivity (λ_{m0}), W/(m·K)	4	Initial thermal conductivity (λ_{b0}), W/(m·K)	8
Permeability (K_{m}), m^2	1×10^{-18}	Permeability (K_{b}), m^2	1×10^{-14}
Initial porosity (φ_{m0})	0.005	Initial porosity (φ_{b0})	0.1
Residual porosity (φ_{mr})	0.005	Residual porosity (φ_{br})	0.003
Internal friction angle (θ_{m}), °	30	Internal friction angle (θ_{b}), °	15
Fluid properties			
Viscosity (μ_{0}), Pa·s	0.002	Density (ρ_{f0}), kg/m^3	1000
Heat capacity (C_{pf}), J/(kg·K)	4200	Thermal conductivity (λ_{f}), W/(m·K)	0.65
Other			
Vertical stress (σ_{V}), MPa	14	Horizontal stress (σ_{h}), MPa	10
Rock temperature (T_{m}), K	393.15	Fluid temperature (T_{f}), K	293.15

of discontinuity, greatly influence the expansion of hydraulic fractures in the fracturing stimulation process. Scholars have investigated the mechanism underlying the influence of the bedding structure on hydraulic fracture extension and reported that when hydraulic fractures extend to the bedding structure, they may undergo behaviors such as arrest, diversion, diversion followed by crossing, and direct crossing (Fig. 6), and these modes are controlled by numerous factors, such as geology and engineering (Fisher and Warpinski, 2012; Gu et al., 2022).

On this basis, in this research, the extension behavior of hydraulic fractures in bedding is simulated. The results are shown in Fig. 7. When a hydraulic fracture extends to the bedding, arrest, diversion, diversion followed by crossing, crossing with simultaneous diversion (crossing and diversion), or direct crossing may occur. When the injection rate of the fracturing fluid is low and the elastic modulus of the rock matrix on both sides of the bedding structure is high, the hydraulic fracture is arrested by the bedding upon reaching it. When the modulus of elasticity of the bedding is much lower than that of the rock matrix and the other parameters remain unchanged, the hydraulic fracture is diverted along the bedding. With increasing principal stress difference, bedding inclination, and elasticity modulus ratio, the hydraulic fracture evolves from diverting along the bedding to directly crossing it. With increasing difference in principal stress and elastic modulus ratio, the behavior of the hydraulic fracture gradually evolves from first diverting along the bedding and then directly crossing the bedding to directly crossing and diverting along the bedding to finally only crossing the bedding. The complex propagation pattern of hydraulic fractures in reservoirs with bedding is considered. In this study, we combine the results of previous studies with the study results for the mechanical properties of the rock, the inclination angle of the bedding, the geostress, etc., and investigate their effects on the propagation behavior of hydraulic fractures in formations with bedding to elucidate the interaction mechanism between shale bedding and hydraulic fractures and its controlling factors.

5.2. Influence of the elastic modulus ratio (E_m/E_f) of the rock matrix on the bedding

Parameters such as the modulus of elasticity, tensile strength, and compressive strength are typically used to represent the mechanical properties of rocks. On this basis, the modulus of elasticity is used to characterize the mechanical properties of rocks in this study. Therefore, the propagation behavior of hydraulic cracks in bedding is analyzed by varying the ratio of the elastic modulus of the rock matrix to that of the bedding (E_m/E_f), thus revealing the influence of the mechanical properties of the rock on the propagation pattern of hydraulic cracks in the bedding. Throughout the simulation process, the other parameters are maintained constant;

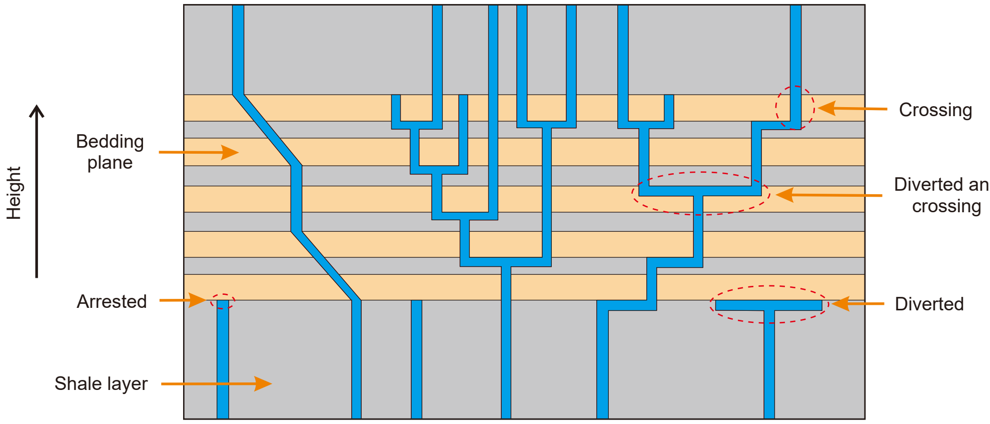

Fig. 6. Hydraulic fracture vertical propagation pattern (Fisher and Warpinski, 2012; Gu et al., 2022).

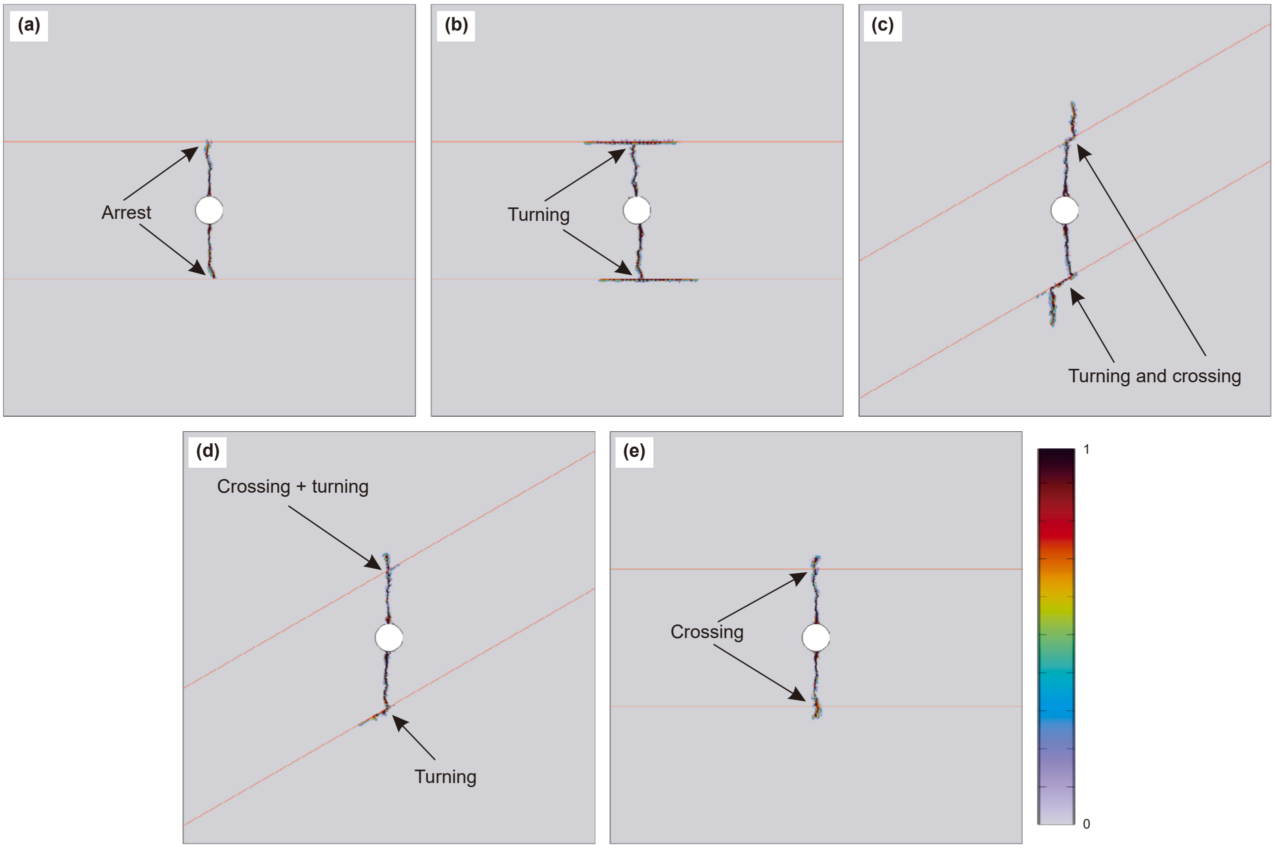

Fig. 7. Extension behavior of hydraulic fractures in bedding. (**a**) Termination, (**b**) turning, (**c**) turning and then crossing, (**d**) turning and crossing, and (**e**) direct crossing.

E_m/E_f is set to 4, 6, 8, or 10; and the corresponding compressive strength and tensile strength are varied proportionally. The simulation results are shown in Fig. 8. When the other parameters are kept constant and E_m/E_f is 4 or 6, the fracturing fluid is injected into the wellbore, and the hydraulic fracture gradually approaches the bedding; it turns along the bedding first, extends along the direction of the bedding for a certain distance, then crosses the bedding directly to enter the upper rock matrix, and finally continues to extend along the vertical stress direction.

Throughout the process, the fracturing fluid exchanges heat with the high-temperature rock, which alters the fracturing fluid properties and modulates the reservoir stimulation effect (Fig. 8(a), (b), (e), (f), (j), and (k)). In addition, the higher the E_m/E_f ratio is, the farther the hydraulic fracture extends along the bedding (Fig. 8(a), (b)). With the increase in E_m/E_f to 8 and 10, the hydraulic fracture extends to the bedding and mainly turns along it, and the fracturing fluid is cut off by the bedding, flows along the direction of the bedding, and exchanges heat with the reservoir, thus increasing the stimulated reservoir volume (Fig. 8(c), (d), (g), (h), (l), and (m)). Therefore, when the other conditions remain unchanged, with increasing difference between the mechanical properties of the rock matrix and the bedding, the extension of the hydraulic fracture to the bedding gradually evolves from directly crossing the bedding to first turning along the bedding and then directly crossing it until it finally only turns along the bedding. In other words, the larger E_m/E_f is, the more favorable the interactions between hydraulic fractures and the bedding are, and the greater the complexity of the generated fracture network, which in turn improves the effect of reservoir stimulation. In addition, the injection of normal-temperature fracturing fluid throughout the whole fracturing process leads to thermal shock and heat exchange of the rock under high temperature and high pressure underground, which alters the viscosity, density, and other properties of the fracturing fluid, thus modulating the effect of reservoir stimulation.

5.3. *Effects of geostress*

Geostress has been demonstrated to notably influence the expansion path of hydraulic fractures and their geometrical morphology in the fracturing process. On this basis, the other parameters are first maintained constant, after which the difference in the vertical principal stress (the difference between the vertical principal stress and the minimum horizontal principal stress) is adjusted to investigate the effects of various geostress states on the propagation pattern of hydraulic fractures in reservoirs with bedding. During the simulation, the difference in vertical stress is set to 4, 8, 12, and 16 MPa, and the simulation results are shown in Fig. 9, in which the other parameters are kept constant, E_m/E_f is 10, and the difference in vertical stress is 4 MPa. The hydraulic fracture extends to the bedding, the fracturing fluid flows across the bedding directly, and some of the fracturing fluid flows along the direction of the bedding, which interacts with the bedding (crossing and turning) (Fig. 9(a)). When the difference in vertical stress increases to 8, 12 and 16 MPa and the hydraulic fracture extends to the bedding, the fracturing fluid directly crosses the bedding and enters the upper rock matrix, after which it flows along the direction of the vertical principal stress (Fig. 9(b), (c) and (d)). Therefore, when the other parameters are kept constant, with increasing difference in vertical stress, the behavior of the hydraulic fracture can be inferred to gradually change from following the bedding to directly crossing the bedding when it

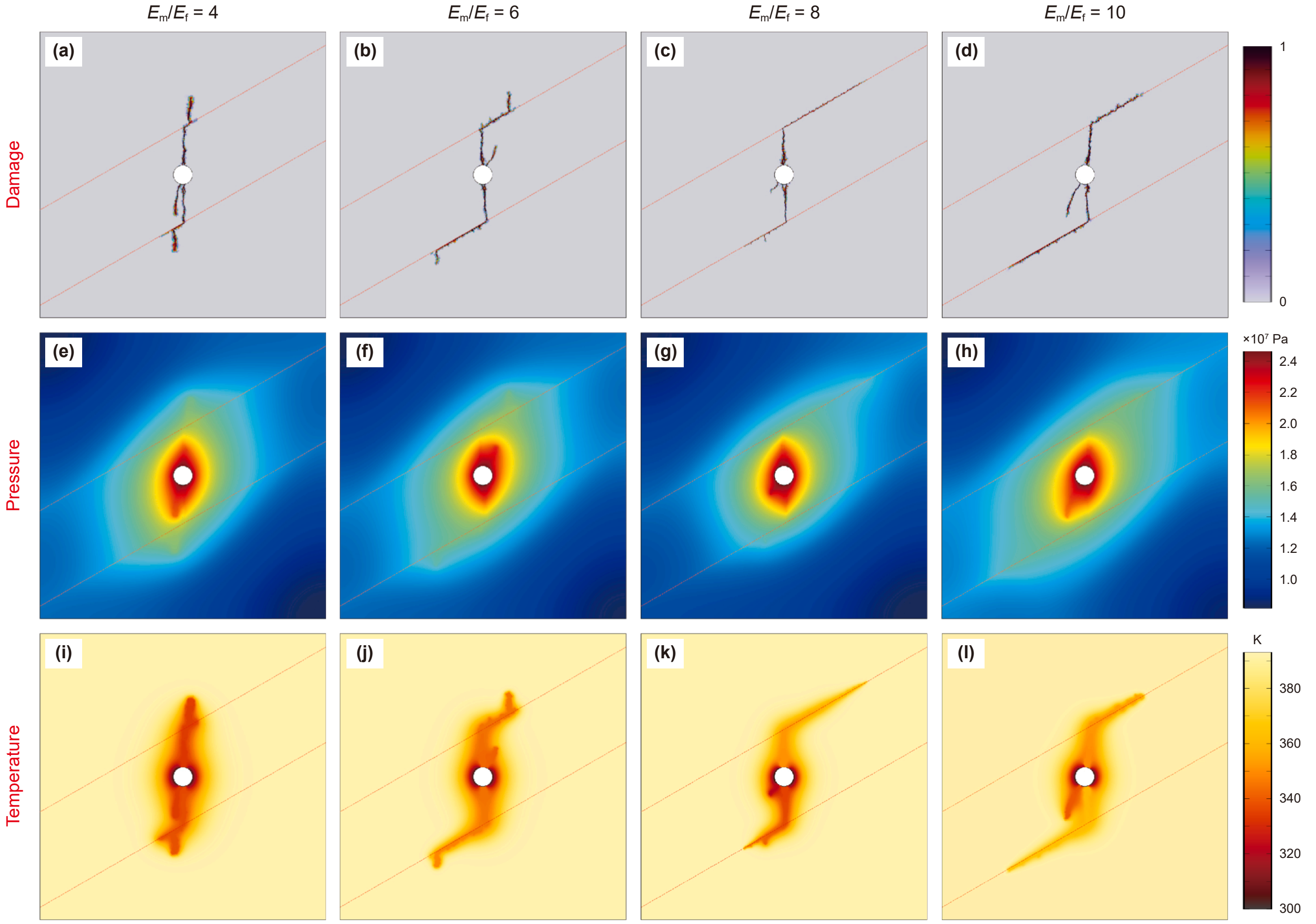

Fig. 8. Extension behavior of hydraulic fractures in reservoirs with bedding at various E_m/E_f ratios. (**a**), (**e**) and (**j**) $E_m/E_f = 4$; (**b**), (**f**), and (**k**) $E_m/E_f = 6$; (**c**), (**g**), and (**l**) $E_m/E_f = 8$; and (**d**), (**h**), and (**m**) $E_m/E_f = 10$.

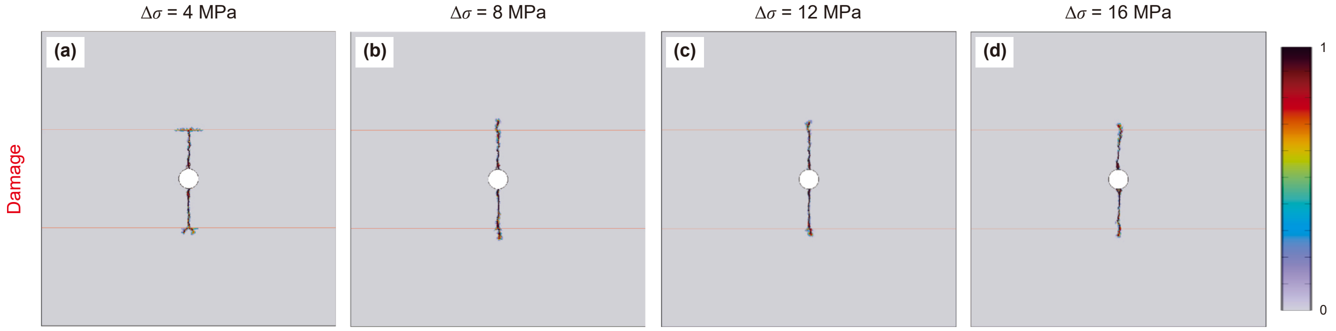

Fig. 9. Extension behavior of hydraulic fractures in bedding with various principal stress differences. (**a**) Principal stress difference of 4 MPa, (**b**) principal stress difference of 8 MPa, (**c**) principal stress difference of 12 MPa, and (**d**) principal stress difference of 16 MPa.

extends to the latter. In other words, the larger the difference in vertical stress is, the more likely the hydraulic fractures are to directly cross the bedding.

Furthermore, the variation in the fluid injection pressure with time during fracturing is analyzed, and the results are shown in Fig. 10. First, the whole fracturing process is divided into stages AB, BC, and CD according to the pressure–time curve, and points E, F, M and N indicate the extension of the hydraulic fracture to the bedding. The difference in vertical stress of 4 MPa is chosen as an example for analysis. Stage AB is the fracturing fluid injection stage, in which the fluid pressure is gradually increased by pumping the fluid into the wellbore until the pressure reaches the rupture pressure of the rock, at which time rock rupture is initiated. The fluid pressure that corresponds to point B is the rupture pressure. Stage BC is the fracture extension stage, in which the rock ruptures at point B because of the accumulated fluid pressure from stage AB. After rupture at point B, the fluid pressure decreases as the fluid acts on the rock, and the hydraulic fracture expands along the vertical principal stress direction until point C is reached, where the fluid energy that acts on the rock reaches its minimum

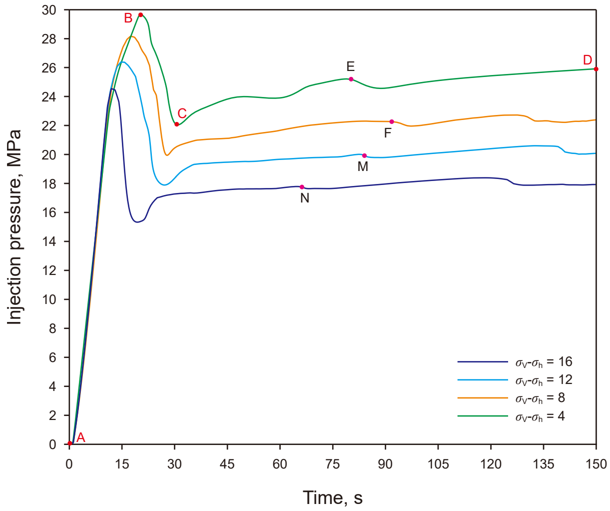

Fig. 10. Variation in the injection pressure over time.

value, as does the corresponding fluid pressure. The unevenness of the curve at this stage occurs because of the heterogeneity of the rock and the difference in the widths of the hydraulic fractures. Stage CD is the crack propagation stage, in which the fluid pressure gradually increases as the rate of increase exceeds that of the crack propagation, and the hydraulic fractures continue to propagate along the direction of the vertical principal stresses. At the same injection rate, the rupture pressures that correspond to differences in vertical stress of 4, 8, 12, and 16 MPa are 29.8, 28.2, 26.8, and 24.4 MPa, respectively, which means that the rupture pressure of the rock gradually decreases with increasing difference in vertical stress, which corresponds to an earlier fracture initiation time. In addition, under the same injection rate, when the difference in vertical stress is 4, 8, 12, and 16 MPa, the time taken for the hydraulic fracture to extend to the bedding is 78, 67, 58 and 49 s, respectively; i.e., as the difference in vertical stress increases, the time needed for the hydraulic fracture to extend to the bedding decreases (points E, F, M, and N in Fig. 10). Thus, when the other conditions are maintained constant, the difference in vertical stress can be inferred to be positively correlated with the distance of hydraulic fracture propagation and negatively correlated with the rupture pressure and fracture initiation time. Additionally, owing to the effects of rock heterogeneity and anisotropy, this conclusion differs across local areas.

5.4. *Effect of the bedding inclination*

Field profile observations indicate that shales are not horizontally stacked. In contrast, most shales intersect the horizontal plane at a certain angle, which results in the shale bedding exhibiting a certain angle of intersection with the horizontal plane. Research has confirmed that the angle of intersection between shale and the horizontal plane (the angle of inclination of the shale) notably influences hydraulic fracture propagation behavior during fracturing. Under different bedding inclination angles, hydraulic fractures exhibit different propagation patterns. On this basis, in this study, while the other parameters are held constant and the E_m/E_f ratio is set to 4, the inclination angles of the bedding are set to 0°, 30°, 45°, and 60° to simulate the extension behavior of hydraulic fractures in reservoirs with bedding structures at various bedding inclination angles. The results are shown in Fig. 11. When the inclination angle of the bedding is 0°, the hydraulic fracture directly crosses the bedding and enters the upper rock matrix when it extends to the bedding (Fig. 11(a)). The fracturing fluid exchanges heat with high-temperature fluid at this time, and the temperature of the fracturing fluid increases and its properties change, which affects the reservoir stimulation results (Fig. 11(e)). As the dip angle of the bedding increases to 30° and 45° when the hydraulic fracture extends to the bedding, the fracture first extends along the bedding for a certain distance and then directly crosses it and enters the upper rock matrix; the greater the dip angle of the bedding is, the further the fracturing fluid flows along the bedding (Fig. 11(b), (c), (f), and (g)). When the inclination angle of the bedding increases to 60°, the fracturing fluid stops at the bedding upon reaching it after initially following the hydraulic fracture and then flows along the direction

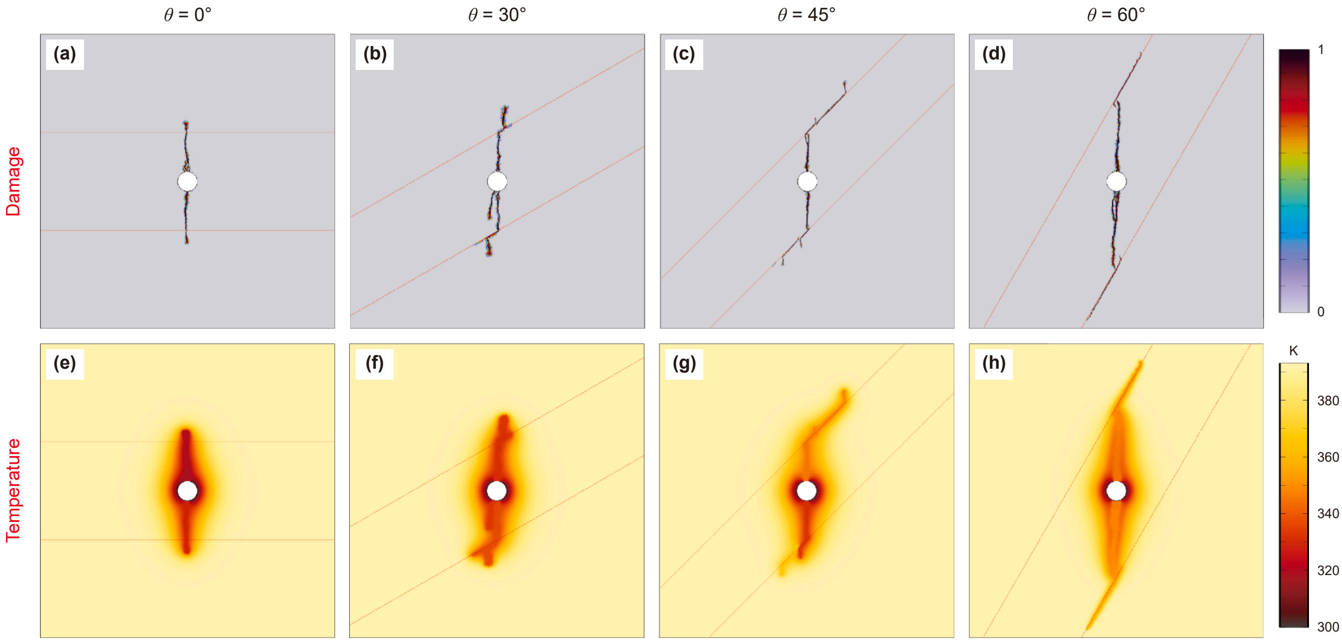

Fig. 11. Expansion behavior of hydraulic fractures in the bedding at various bedding dip angles. (**a**) Bedding inclination angle of 0°, (**b**) bedding inclination angle of 30°, (**c**) bedding inclination angle of 45°, and (**d**) bedding inclination angle of 60°.

of the bedding, and the bedding is reactivated (Fig. 11(d), (h)). When the other parameters are maintained constant, with increasing inclination angle of the bedding, the hydraulic fracture propagation to the bedding gradually evolves from directly crossing the bedding to turning along the bedding and then directly crossing the bedding until the fracture finally propagates only along the direction of the bedding. In other words, the higher the inclination angle of the bedding, the more favorable the extension of hydraulic fractures along the bedding is. In addition, when hydraulic fractures first turn along the bedding and then directly cross it, the greater the bedding inclination angle is, the farther the hydraulic fractures extend along the bedding.

5.5. *Effect of temperature*

With increasing shale reservoir depth, the reservoir temperature gradually increases, which leads to changes in the mechanical properties of the rock, pore structure, and other characteristics, which in turn affect the reservoir stimulation results. Moreover, temperature change affects the properties of the fracturing fluid, which in turn affects hydraulic fracture extension. On this basis, the other parameters are kept constant in this study, E_m/E_f is 10, the injected fluid temperature is 293.15 K, and the reservoir temperature is set to 353.15, 373.15, 393.15, and 413.15 K to investigate the propagation pattern of hydraulic fractures in reservoirs with bedding at various temperatures. The results are shown in Fig. 12. When the other parameters are maintained constant and the reservoir temperature is 353.15 K, the hydraulic fracture directly crosses the bedding and enters the upper rock matrix when it extends to it; at this time, heat exchange between the fracturing fluid and the reservoir rock occurs, the temperature of the fracturing fluid gradually increases, and the properties of the fracturing fluid, such as the density and viscosity, change, which affects the reservoir stimulation results (Fig. 12(a) and (e)). As the reservoir temperature increases to 373.15 K, when the hydraulic fracture extends to the bedding, it may cross the latter directly, and while crossing the bedding, the fracturing fluid flows along the direction of the bedding, which activates the bedding (Fig. 12(b), (f)). As the temperature is increased to 393.15 K, the hydraulic fractures approaches and eventually crosses the bedding, and simultaneously, the fracturing fluid flows along the bedding, thus activating the bedding (Fig. 12(c), (g)). When the temperature increases to 413.15 K, the hydraulic fracture extends to the bedding and then turns along it or directly crosses it, thus activating the bedding and increasing the reservoir stimulation volume (Fig. 12(d), (h)). At this time, there is a difference in the propagation pattern of the hydraulic fracture between the upper and lower sides of the bedding plane, which is caused by the heterogeneity in the rock (Fig. 12(d), (h)). According to the results, in the fracturing process, when other parameters are maintained constant, with increasing reservoir depth, the temperature in the reservoir gradually increases, and when the hydraulic fracture extends to the bedding, the behavior of the hydraulic fracture gradually develops from directly crossing the bedding to turning along it while crossing it, and with a further increase in temperature, the hydraulic fracture only turns along the bedding in the end. In other words, an increase in reservoir rock temperature promotes the turning of hydraulic fractures along the bedding and the generation of more discontinuities, thus increasing the reservoir stimulation volume.

Afterward, the wellbore pressure and temperature changes during fracturing are analyzed. As shown in Fig. 13, adopting the reservoir temperature of 413.15 K as an example, the fracturing process can be divided into stages HI, IJ, and JK according to the curve of the change in the wellbore temperature. Stage HI is the stage during which the wellbore temperature rapidly decreases. In this stage, with the continuous injection of fluid pressure, the wellbore temperature decreases rapidly until the minimum value of 312.17 K is reached at 15 s. Stage IJ is the stage in which the wellbore temperature rapidly increases. At this stage, with the continuous injection of fracturing fluid, the wellbore pressure increases until it reaches the rupture pressure, and then the reservoir starts to crack, and with increasing fluid–rock contact surface, the fluid temperature increases faster until it reaches point J. At this time, the rate of injection of the fracturing fluid is more consistent with the rate of fluid warming. At stage JK, the temperature in the wellbore changes more slowly. Compared with the previous two stages, the wellbore

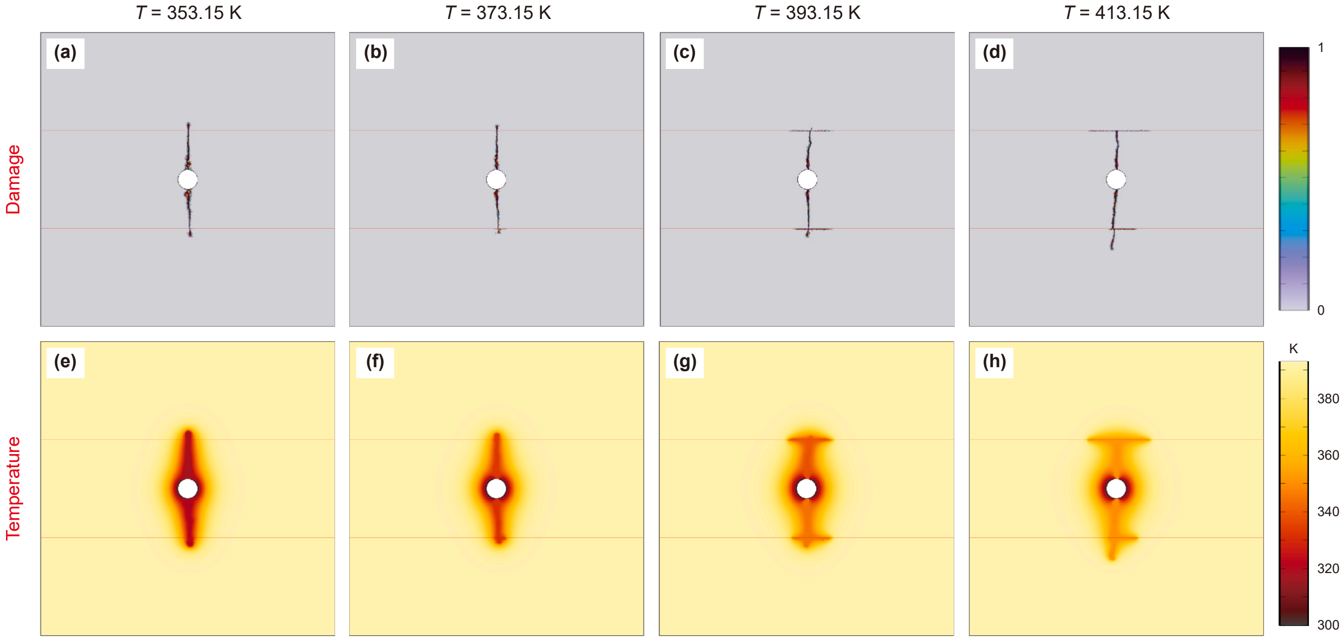

Fig. 12. Extension behavior of hydraulic cracks in bedding at various temperatures. (**a**) and (**e**) $T = 353.15$ K, (**b**) and (**f**) $T = 373.15$ K, (**c**) and (**g**) $T = 393.15$ K, and (**d**) and (**h**) $T = 413.15$ K.

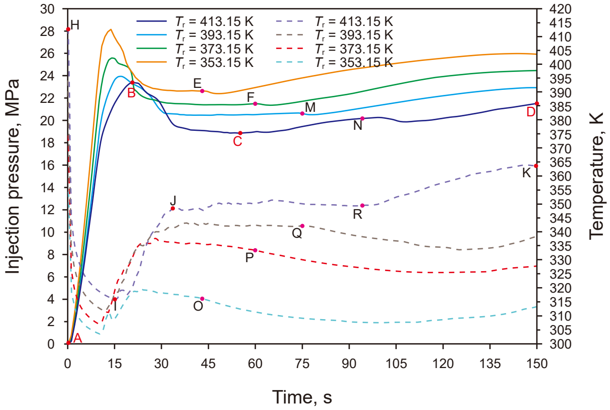

Fig. 13. Variation in the fluid pressure with time at various reservoir temperatures.

temperature at this stage increases or decreases with time, but the rate of increase or decrease is low, which indicates that the fluid injection rate and the fracturing fluid warming rate are more consistent at this time, and the gradual curve fluctuations are caused by the heterogeneity in the rock. In addition, at stage HI, the times to reach point I (lowest temperature) at reservoir temperatures of 353.15, 373.15, 393.15, and 413.15 K are 10, 11, 12 and 15 s, respectively, and the corresponding real-time temperatures are 304.21, 307.87, 310.57 and 312.17 K, respectively. When the other parameters are kept constant, with increasing reservoir temperature, the time needed to reach its minimum temperature increases, and the corresponding minimum temperature also increases. In addition, the time required for its extension to the bedding is analyzed. O, P, Q, and R in Fig. 13 indicate the times required for hydraulic fractures to extend to the bedding at reservoir temperatures of 353.15, 373.15, 393.15, and 413.15 K, which are 42, 60, 75, and 99 s, respectively. Thus, the time necessary for hydraulic fractures to extend to the bedding increases with increasing reservoir temperature when the other parameters are kept constant. An increase in temperature leads to decreases in the viscosity and density of the fracturing fluid, which in turn reduces the energy of the fracturing fluid, thus leading to an increase in the time needed for the fracture to extend the same distance.

The fluid pressure change curve is similar to that in Fig. 10. Therefore, only its relationship with temperature is analyzed here. Fig. 13 reveals that the time needed to reach point B (rupture pressure) is 14, 15, 17, and 21 s under reservoir temperatures of 353.15, 373.15, 393.15, and 413.15 K, respectively. The corresponding rupture pressures are 28.05, 25.33, 23.91, and 23.20 MPa, respectively, and the rupture pressure of the reservoir rock gradually decreases with increasing reservoir temperature. With increasing reservoir temperature, the rupture pressure of the reservoir rock decreases gradually, and the time needed to reach the rupture pressure increases gradually. The rock comprises many types of minerals, and different minerals exhibit distinct expansion capacities. When the reservoir temperature increases, the expansion of different minerals differs, thereby resulting in microcracks between minerals, which decreases the strength of the rock, and the corresponding rupture pressure decreases accordingly. The reservoir temperature is negatively correlated with the rock fracture pressure.

5.6. Criteria for hydraulic fracture propagation under the action of various factor combinations

(1) Criteria for hydraulic fracture propagation under combinations of two factors

First, the results of previous studies reveal that the ratio of the elastic moduli of the rock matrix and bedding, geostress, bedding inclination, and temperature notably influence the propagation pattern of hydraulic fractures in the bedding. On this basis, these four influencing factors are combined in pairs to analyze the propagation behavior of hydraulic fractures in the bedding under the effects of various factor combinations. The results are shown in Fig. 14, in which the graphical area is divided according to four propagation patterns: direct crossing, turning, turning and then crossing, and crossing and diverting. When the other parameters are maintained constant and E_m/E_f does not change, with increasing difference in vertical stress, hydraulic fractures tend to directly cross the bedding when they extend to the bedding. When the difference in vertical stress is greater than or equal to 16 MPa, hydraulic fractures that extend to the bedding directly cross the bedding (Fig. 14(a)). In contrast, increases in bedding inclination and temperature are favorable for the turning of the hydraulic fractures along the bedding. When the bedding dip angle is greater than or equal to 60° or the E_m/E_f ratio is greater than or equal to 6 and the temperature is greater than or equal to 413.15 K, hydraulic fractures that extend to the bedding divert along the bedding (Fig. 14(b), (c)). When the other parameters are kept constant, the difference in vertical stress is kept constant, and the temperature is greater than or equal to 413.15 K, hydraulic fractures tend to propagate along bedding when they reach the bedding (Fig. 14(d)). Additionally, a bedding dip angle greater than or equal to 60° favors the propagation of hydraulic fractures along the bedding (Fig. 14(e)). For combinations of the temperature and bedding inclination angle, when the other parameters are kept constant and the bedding inclination angle is set to a specific value greater than or equal to 60°, as the temperature increases to 393.15 K, hydraulic fractures that extend to the bedding are more likely to divert along the bedding (Fig. 14(f)). With the other factors held constant, increases in the bedding dip angle, temperature, and elastic modulus ratio are favorable for hydraulic fracture diversion along the bedding. Specifically, when the bedding dip angle is greater than or equal to 60°, the temperature is greater than or equal to 413.15 K, and the elastic modulus ratio is greater than or equal to 6, hydraulic fractures are more likely to be diverted along the bedding; conversely, an increase in the difference in vertical stress favors hydraulic fractures directly crossing the bedding, and the difference in vertical stress being greater than or equal to 16 MPa favors hydraulic fractures directly crossing the bedding.

(2) Criteria for hydraulic fracture propagation under combinations of three factors

On the basis of the results of two-by-two combination analysis, the propagation pattern of hydraulic fractures in reservoirs with bedding under the effects of combinations of three factors, namely, the elastic modulus ratio–vertical stress difference–bedding inclination, elastic modulus ratio–vertical stress difference–temperature, bedding inclination–temperature–elastic modulus ratio, and bedding inclination–temperature–vertical stress difference, are analyzed. The specific steps are as follows: first, while the other parameters are kept constant, the first two and the last two parameters are used as vertical and horizontal coordinates, respectively, of the elastic modulus ratio–vertical stress difference and bedding inclination–temperature, and the bedding inclination, temperature, elastic modulus ratio, and vertical stress difference are changed in turn to investigate the extension mechanism of hydraulic fractures in reservoirs with bedding under this combination of the three factors. The results are shown in Fig. 15, and the image area is divided according to the propagation pattern of hydraulic fractures in the bedding. As shown in Fig. 15(a), when the inclination

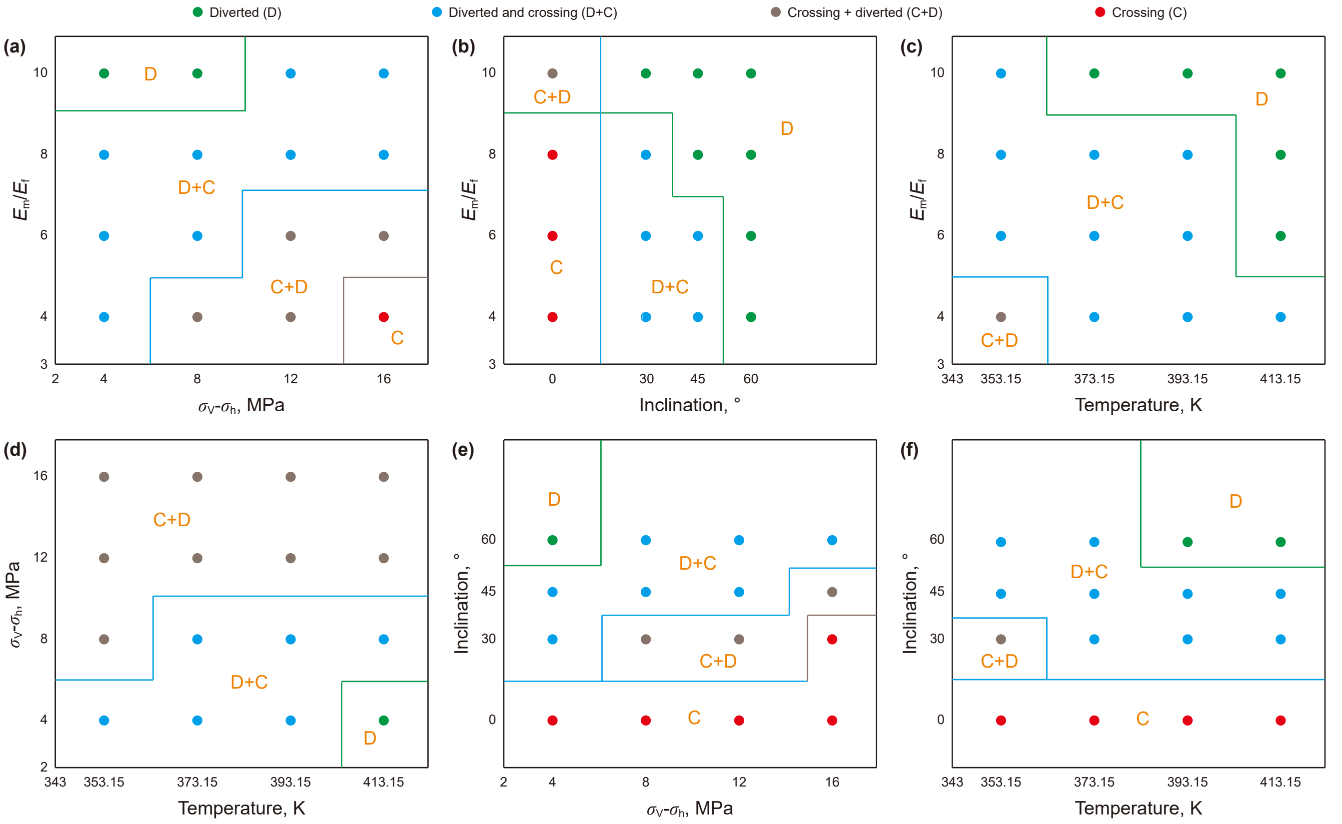

Fig. 14. Extension criterion for hydraulic fractures in bedding under the combined action of two influencing factors. (**a**) Constant temperature and bedding inclination, (**b**) constant temperature and difference in vertical stress, (**c**) constant bedding inclination and difference in vertical stress, (**d**) constant bedding inclination and E_m/E_f, (**e**) constant temperature and E_m/E_f, and (**f**) constant E_m/E_f and difference in vertical stress.

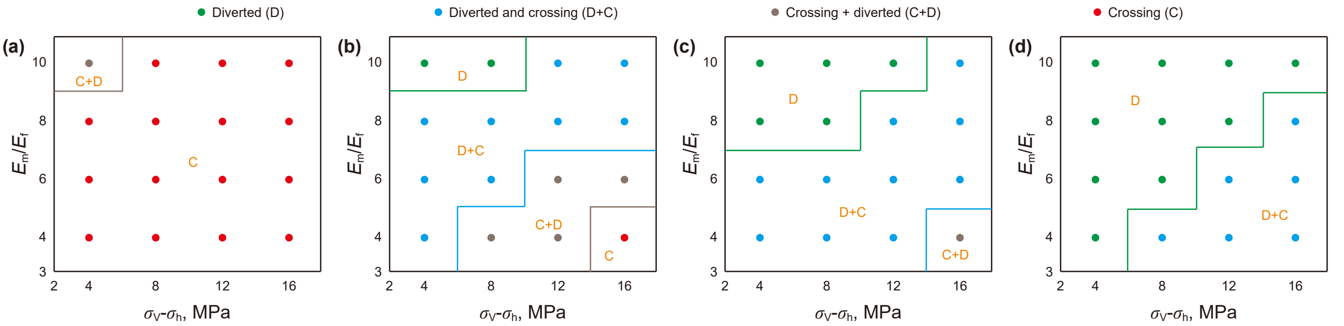

Fig. 15. Extension behavior of hydraulic fractures in bedding at various bedding inclinations. (**a**) Bedding inclination angle of 0°, (**b**) bedding inclination angle of 30°, (**c**) bedding inclination angle of 45°, an (**d**) bedding inclination angle of 60°.

angle of the bedding is 0°, the difference in vertical stress is less than or equal to 4 MPa, and when E_m/E_f is greater than or equal to 10, the hydraulic fracture turns along the bedding while crossing the bedding upon reaching it; when the difference in vertical stress is greater than 4 MPa or less than E_m/E_f is less than 10, the hydraulic fracture directly crosses the bedding when it reaches the latter. As the dip angle of the bedding increases to 30°, 45°, and 60°, the propagation pattern of hydraulic fractures becomes complicated when they extend into the bedding. Additionally, the proportion of the area where the hydraulic fracture directly crosses the bedding gradually decreases to 0, and the proportion of the area where the hydraulic fracture is diverted along the bedding gradually increases; i.e., an increase in bedding inclination is favorable for the diversion of hydraulic fractures along the bedding (Fig. 15(b), (c), and (d)). Similarly, an analysis of the data in Fig. 16 reveals that when the other parameters are kept constant and E_m/E_f and the difference in vertical stress are the vertical and horizontal coordinates, with increasing temperature, when the hydraulic fracture extends to the bedding, the proportion of the area where the hydraulic fracture is diverted along the bedding gradually increases, and the proportion of the area where the hydraulic fracture directly crosses through the bedding gradually decreases or even becomes zero, which indicates that an increase in temperature favors the diversion of hydraulic fractures along the bedding. Afterward, taking the bedding inclination temperature as the vertical and horizontal coordinates, E_m/E_f is 4, 6, 8, and 10, and with increasing E_m/E_f ratio, the proportion of the area that is diverted along the bedding gradually increases and the proportion of the area where the hydraulic fracture directly crosses the bedding gradually decreases when the hydraulic fracture extends to the bedding, which indicates that an increase in the ratio of the elastic moduli of the rock matrix and bedding is favorable for the diversion of hydraulic fractures along the bedding

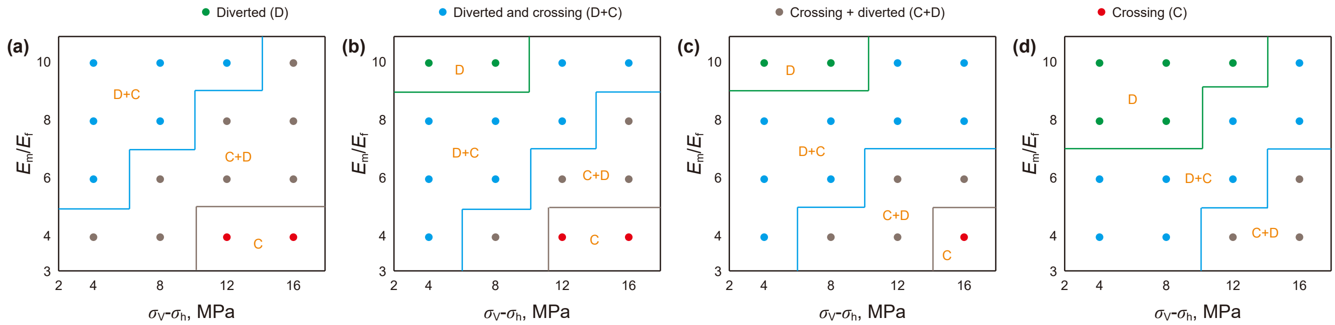

Fig. 16. Extension behavior of hydraulic fractures in bedding at various temperatures. (**a**) $T = 353.15$ K, (**b**) $T = 373.15$ K, (**c**) $T = 393.15$ K, and (**d**) $T = 413.15$ K.

(Fig. 17). In addition, when the other parameters are kept constant and the difference in vertical stress is set to 4, 8, 12 and 16 MPa, as the difference in vertical stress increases, more hydraulic fractures that extend to the bedding cross the bedding directly, and the corresponding percentage of the area gradually increases, while the percentage of the area where the hydraulic fracture is diverted along the bedding gradually decreases (Fig. 18). An increase in the difference in vertical stress is favorable for the crossing of hydraulic fractures through the bedding and their entry into the upper rock matrix.

6. Effect of the bedding structure on hydraulic fracture propagation

In Section 5, the propagation patterns of hydraulic fractures in individual bedding planes were analyzed. Observations revealed that shale develops a massive bedding structure, and on this basis, the extension behavior of hydraulic fractures in shale bedding when a massive bedding structure is well developed is investigated, and the mechanism of the influence of the bedding structure on the extension behavior of hydraulic fractures is clarified.

6.1. *Effect of the elastic modulus ratio (E_m/E_f) of the rock matrix and the bedding*

Shales contain numerous bedding structures, on the basis of which the extension behavior of hydraulic fractures in well-bedded shales is simulated in this study via an established numerical model. In this study, the model is set with a spacing of 10 mm between the bedding planes, the other parameters are kept constant, and E_m/E_f is set to 4, 6, 8, and 10 to investigate the extension behavior of hydraulic fractures in shale with developed bedding. The results are shown in Fig. 19, in which the red lines indicate the bedding; when the shale bedding is developed, the propagation pattern of hydraulic fractures extending to the bedding mainly occurs, such as direct crossing, diversion, crossing and diversion, and diversion before crossing. When the other parameters are kept constant and E_m/E_f is 4, the hydraulic fractures extend vertically to the bedding, and they cross the bedding directly or are diverted along the bedding for a certain distance first and then cross the bedding directly to enter the upper rock matrix (Fig. 19(a)); as E_m/E_f gradually increases to 6 and 8, the hydraulic fractures extend to the bedding, and in addition to crossing the bedding directly, they also cross the bedding and divert along the bedding at the same time (Fig. 19(b), (c)). When E_m/E_f increases to 10, the hydraulic fractures are mainly diverted along the bedding and cross and are eventually diverted when they extend to the latter (Fig. 19(d)). Therefore, for shale with well-developed bedding, when the other parameters are kept constant, with increasing elastic modulus ratio between the rock matrix and bedding, the extension of hydraulic fractures to the bedding easily evolves from directly crossing the bedding to crossing and gradually diverting until they only divert along the bedding. In addition, when a hydraulic fracture experiences crossing and diverting behavior in the bedding, the larger the E_m/E_f ratio is, the farther the hydraulic fracture diverts along the bedding. Notably, the greater the ratio of the elastic moduli of the rock matrix and bedding, the more favorable the diversion of the hydraulic fracture along the bedding and the flowing of the fracturing fluid along the bedding direction are, which results in the reactivation of the bedding and the generation of more discontinuities, thus increasing the volume of the reservoir stimulation.

6.2. *Effect of the injection rate on hydraulic fracture propagation*

In accordance with Section 6.1, with the other parameters kept unchanged and E_m/E_f set to 8, simulations are conducted to study the propagation behaviors of hydraulic fractures under various

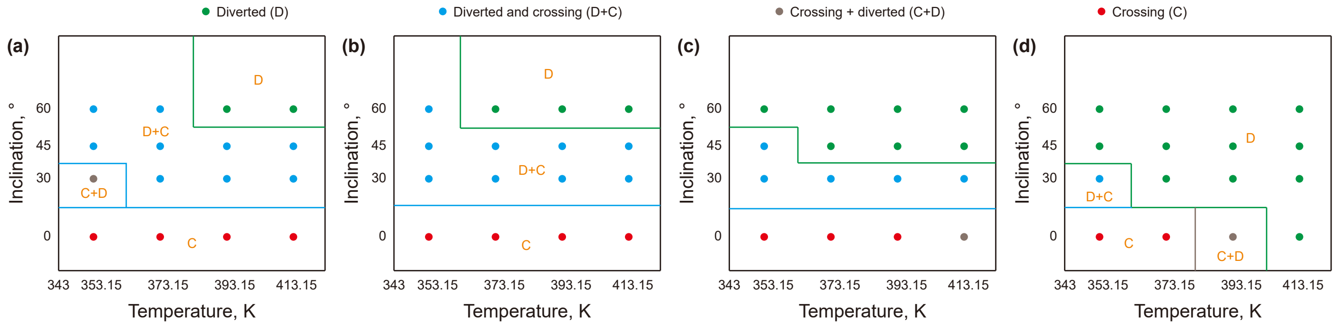

Fig. 17. Extension behavior of hydraulic fractures in bedding at various values of E_m/E_f. (**a**) $E_m/E_f = 4$, (**b**) $E_m/E_f = 6$, (**c**) $E_m/E_f = 8$, and (**d**) $E_m/E_f = 10$.

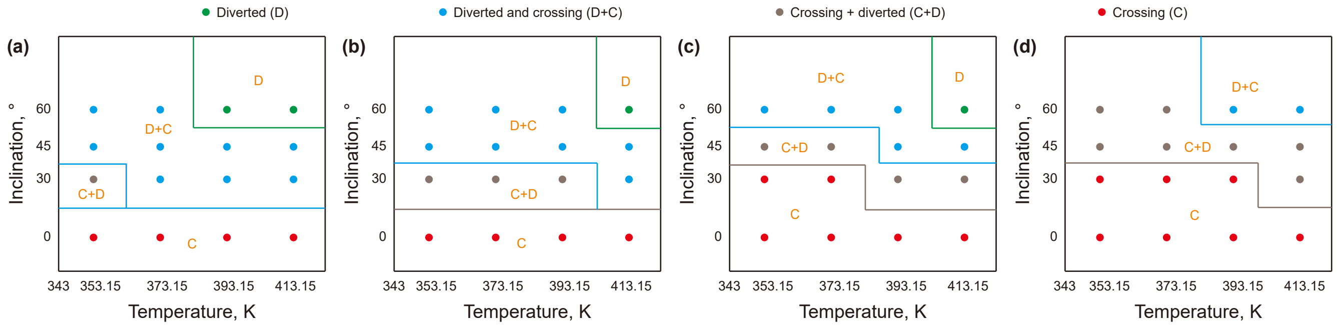

Fig. 18. Extension behavior of hydraulic fractures in bedding with various differences in vertical stress. (**a**) The difference in vertical stress is 4 MPa, (**b**) the difference in vertical stress is 8 MPa, (**c**) the difference in vertical stress is 12 MPa, and (**d**) the difference in vertical stress is 16 MPa.

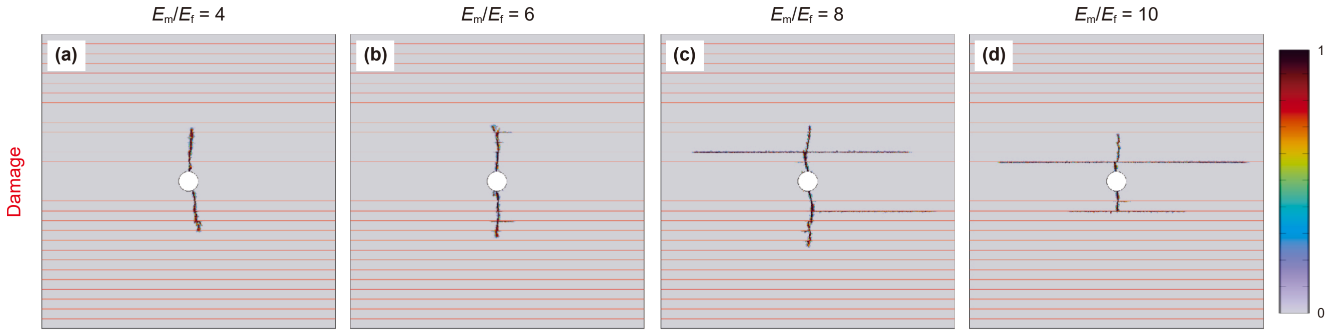
E_m/E_f = 4

E_m/E_f = 6

E_m/E_f = 8

E_m/E_f = 10

Fig. 19. Extension behavior of hydraulic fractures in bedding at various E_m/E_f values. (**a**) $E_m/E_f = 4$, (**b**) $E_m/E_f = 6$, (**c**) $E_m/E_f = 8$, and (**d**) $E_m/E_f = 10$.

fracturing fluid injection rates. In the simulation process, the fracturing fluid injection rate is set to 3×10^{-7}, 4×10^{-7}, 5×10^{-7}, and 6×10^{-7} m^3/s in succession, and the simulation results are shown in Fig. 20. When the bedding is developed, the hydraulic fracture extends to the bedding and may cross the bedding directly or cross and be diverted along it. When the other parameters are kept constant, the fracturing fluid injection rate is 3×10^{-7} or 4×10^{-7} m^3/s; when the hydraulic fracture extends to the bedding, it directly crosses the bedding or diverts along the bedding while crossing it, and the fracturing fluid exchanges heat with the reservoir rock and changes its properties, which in turn modulates the reservoir stimulation effect (Fig. 20(a), (b), (e), and (f)). As the

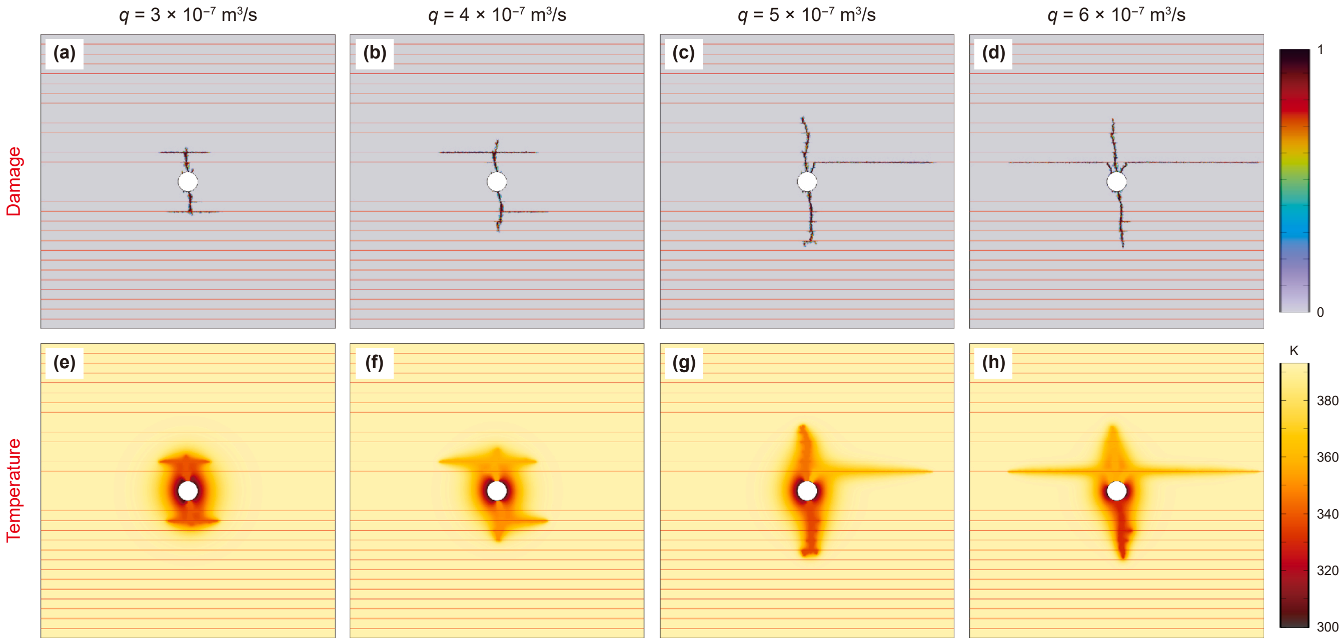
$q = 3 \times 10^{-7}$ m^3/s

$q = 4 \times 10^{-7}$ m^3/s

$q = 5 \times 10^{-7}$ m^3/s

$q = 6 \times 10^{-7}$ m^3/s

Fig. 20. Extension behavior of hydraulic fractures in bedded structures at various injection rates. (**a**) and (**e**) with an injection rate of 3×10^{-7} m^3/s, (**b**) and (**f**) with an injection rate of 4×10^{-7} m^3/s, (**c**) and (**g**) with an injection rate of 5×10^{-7} m^3/s, and (**d**) and (**h**) with an injection rate of 6×10^{-7} m^3/s.

fracturing fluid injection rate increases to 5×10^{-7} or 6×10^{-7} m^3/s, the wellbore is subjected to fluid pressure and starts to crack, which results in the formation of multiple hydraulic fractures (Fig. 20(c) and (d)). When the main fracture extends to the bedding, it directly crosses it or is diverted along it while also crossing it, and the extension distance along the bedding is smaller than the extension distances that correspond to injection rates of 3×10^{-7} and 4×10^{-7} m^3/s; when the branching fracture extends to the bedding, the fracturing fluid flows along the direction of the bedding, and the bedding is activated, which in turn increases the reservoir stimulation volume (Fig. 20). A comprehensive analysis reveals that when the hydraulic fracture passes through the bedding and is diverted along it simultaneously, the extension distance of the hydraulic fracture along the bedding decreases with increasing fracturing fluid injection rate; moreover, the higher the fracturing fluid injection rate is, the shorter the time needed for the hydraulic fracture to extend to the first bedding, and the hydraulic fracture crosses the bedding directly when it reaches the latter. A higher injection rate causes the fracturing fluid to contain more energy, and it can flow across a larger distance.

7. Conclusions

The focus of this study was shale with well-developed bedding. On the basis of theories such as rock mechanics, fracture mechanics, damage mechanics, maximum tensile stress, and Mohr–Coulomb theory and considering rock deformation, fluid flow, and heat transfer phenomena, a coupled thermal–hydraulic–mechanical finite element numerical model was established at the hydraulic fracturing experimental scale. By simulating the hydraulic fracturing process of shale, the following primary conclusions were obtained:

(1) A comparison of the results of previous hydraulic fracturing experiments and numerical results with the results obtained with this model revealed that the two sets of results suitably agreed, thereby validating the reliability of the model.
(2) The results of this study indicated that when hydraulic fractures propagate into shale bedding, five propagation modes may occur: arrest, diversion, diversion followed by crossing, crossing and diversion, and direct crossing. These modes are influenced by factors such as the geostress, rock mechanical properties, bedding plane dip angle, reservoir temperature, and fracturing fluid injection rate.
(3) As the ratio of the elastic moduli of the rock matrix and bedding, the bedding dip angle, and the temperature increase, hydraulic fractures are diverted along the bedding when they extend into the latter. When the bedding dip angle is greater than or equal to 60°, the temperature is greater than or equal to 413.15 K, and the elastic modulus ratio is greater than or equal to 6, the diversion of hydraulic fractures along the bedding is more favorable. As the principal stress difference and hydraulic fracturing fluid injection rate increase, hydraulic fractures typically directly cross the bedding when they expand into it. When the difference in principal stress is greater than 16 MPa, direct crossing of the bedding by hydraulic fractures is more favorable.
(4) For shale with a well-developed bedding structure, with increasing ratio of the elastic moduli of the rock matrix and bedding structure, when the hydraulic fracture extends to the bedding structure, the number of hydraulic fractures that cross the bedding structure directly decreases, and the hydraulic fractures are diverted along the bedding structure close to the wellbore.

CRediT authorship contribution statement

Xun Gong: Writing – review & editing, Writing – original draft, Visualization, Validation, Software, Methodology, Investigation, Formal analysis, Conceptualization. **Zhi-Jun Jin:** Writing – review & editing, Supervision, Resources, Methodology, Funding acquisition, Conceptualization. **Xin-Hua Ma:** Writing – review & editing, Supervision, Methodology, Funding acquisition, Conceptualization. **Yu-Yang Liu:** Writing – review & editing, Supervision, Methodology, Funding acquisition, Conceptualization. **Yan-Jun Guo:** Writing – review & editing, Supervision. **Mei-Zhu Wang:** Writing – review & editing, Supervision.

Declaration of competing interests

The authors declare that they have no known competing financial interests or personal relationships that could have appeared to influence the work reported in this paper.

Acknowledgments

This work was supported by the National Key Technology Research and Development Program of the Ministry of Science and Technology of China (No. 2025ZD1401403-04) and the PetroChina's Fundamental Prospective Project (Nos. 2024DJ8705, 2023ZZ08 and 2024DJ23), which are gratefully acknowledged.

References

Blanton, T.L., 1982. An experimental study of interaction between hydraulically induced and pre-existing fractures. In: SPE Unconventional Resources Conference/Gas Technology Symposium. SPE 1982, SPE-10847-MS. https://doi.org/10.2118/10847-MS.

Blanton, T.L., 1986. Propagation of hydraulically and dynamically induced fractures in naturally fractured reservoirs. In: SPE Unconventional Resources Conference/Gas Technology Symposium. SPE 1986, SPE-15261-MS. https://doi.org/10.2118/15261-MS.

Chalmers, G.R., Bustin, R.M., Power, I.M., 2012. Characterization of gas shale pore systems by porosimetry, pycnometry, surface area, and field emission scanning electron microscopy/transmission electron microscopy image analyses: Examples from the Barnett, Woodford, Haynesville, Marcellus, and Doig units. AAPG Bull. 96 (6), 1099–1119. https://doi.org/10.1306/10171111052.

Chen, B., Barboza, B.R., Sun, Y., et al., 2021. A review of hydraulic fracturing simulation. Arch Comput. Method E 2021, 1–58. https://doi.org/10.1007/s11831-021-09653-z.

Cheng, L., Luo, Z., Xie, Y., et al., 2023. Numerical simulation and analysis of damage evolution and fracture activation in enhanced tight oil recovery using a THMD coupled model. Comput. Geotech. 155, 105244. https://doi.org/10.1016/j.compgeo.2023.105244.

Clarkson, C.R., Solano, N., Bustin, R.M., et al., 2013. Pore structure characterization of North American shale gas reservoirs using USANS/SANS, gas adsorption, and mercury intrusion. Fuel 103, 606–616. https://doi.org/10.1016/j.fuel.2012.06.119.

Cong, R., Yang, R., Jing, M., et al., 2024. Experimental investigation on hydraulic fracture propagation behaviors of coal-measure thin interbedded rocks. Rock Mech. Rock Eng. 57, 1–17. https://doi.org/10.1007/s00603-024-04013-2.

Cundall, P.A., Strack, O., 2008. A discrete numerical model for granular assemblies. Geotechnique 30 (3), 331–336. https://doi.org/10.1680/geot.1979.29.1.47.

Fisher, K., Warpinski, N., 2012. Hydraulic-fracture-height growth: Real data. SPE Prod. Oper. 27 (1), 8–19. https://doi.org/10.2118/145949-PA.

Fu, W., Morris, J.P., Fu, P., et al., 2020. Simulating tightly-spaced swarming hydraulic fractures at field scale using an upscaling approach. In: Proceedings of the ARMA US Rock Mechanics/Geomechanics Symposium. ARMA. 2020, ARMA-2020-1044.

Gong, X., Jin, Z.J., Ma, X.H., et al., 2025b. Effect of bedding structures on hydraulic fracture propagation behavior investigated using a coupled thermo-hydraulic-mechanical numerical model based on the phase-field cohesive zone method. Comput. Geotech. 186, 107427. https://doi.org/10.1016/j.compgeo.2025.107427.

Gong, X., Jin, Z.J., Ma, X.H., et al., 2025a. Simulation investigation of hydraulic fracture propagation patterns at lithological interfaces based on the phase-field method. Rock Mech. Rock Eng. 58 (3), 2803–2828. https://doi.org/10.1007/s00603-024-04258-x.

Gong, X., Ma, X.H., Liu, Y.Y., 2024. Analysis of geological factors affecting propagation behavior of fracture during hydraulic fracturing shale formation. Geomech. Geophys. Geo-energ. Geo-resour. 10 (1), 102. https://doi.org/10.1007/s40948-024-00819-0.

Gu, H., Weng, X., Lund, J., et al., 2012. Hydraulic fracture crossing natural fracture at nonorthogonal angles: a criterion and its validation. SPE Prod. Oper. 27 (1), 20–26. https://doi.org/10.2118/139984-MS.

Gu, M., Li, G., Cheng, S., et al., 2022. Laboratory imaging of 2D hydraulic fracture propagation in laminated shale. In: 56th U.S. Rock Mechanics/Geomechanics Symposium. https://doi.org/10.56952/ARMA-2022-0150.

Guo, T., Tang, S., Liu, S., et al., 2021. Physical simulation of hydraulic fracturing of large-sized tight sandstone outcrops. SPE J. 26 (1), 372–393. https://doi.org/10.2118/204210-PA.

Guo, T., Zhang, S., Qu, Z., et al., 2014. Experimental study of hydraulic fracturing for shale by stimulated reservoir volume. Fuel 128, 373–380. https://doi.org/10.1016/j.fuel.2014.03.029.

Hou, B., Zhang, R., Zeng, Y., et al., 2018. Analysis of hydraulic fracture initiation and propagation in deep shale formation with high horizontal stress difference. Geoenergy Sci. Eng. 170, 231–243. https://doi.org/10.1016/j.petrol.2018.06.060.

Hu, L., Ghassemi, A., 2021. Laboratory-scale investigation of the slippage of a natural fracture resulting from an approaching hydraulic fracture. Rock Mech. Rock Eng. 54, 2547–2558. https://doi.org/10.1007/s00603-021-02398-y.

Jarvie, D.M., Hill, R.J., Ruble, T.E., et al., 2007. Unconventional shale-gas systems: the Mississippian Barnett Shale of north-central Texas as one model for thermogenic shale-gas assessment. AAPG Bull. 91 (4), 475–499. https://doi.org/10.1306/12190606068.

Jiang, Y., Liang, W., Cai, T., et al., 2023. Fracture growth and acoustic emission response in natural coal-rock blocks with different stress, fracturing medium and injection rates. Geoenergy Sci. Eng. 220, 111228. https://doi.org/10.1016/j.petrol.2022.111228.

Ju, Y., Wang, Y., Xu, B., et al., 2019. Numerical analysis of the effects of bedded interfaces on hydraulic fracture propagation in tight multilayered reservoirs considering hydro-mechanical coupling. J. Pet. Sci. Eng. 178, 356–375. https://doi.org/10.1016/j.petrol.2019.03.049.

Lecampion, B., Bunger, A., Zhang, X., 2018. Numerical methods for hydraulic fracture propagation: A review of recent trends. J. Nat. Gas Sci. Eng. 49, 66–83. https://doi.org/10.1016/j.jngse.2017.10.012.

Lei, B., Zuo, J., Coli, M., et al., 2024. Investigation on failure behavior and hydraulic fracturing mechanism of Longmaxi shale with different bedding properties. Comput. Geotech. 167, 106081. https://doi.org/10.1016/j.compgeo.2024.106081.

Lei, Q., Doonechaly, N.G., Tsang, C.F., 2021. Modelling fluid injection-induced fracture activation, damage growth, seismicity occurrence and connectivity change in naturally fractured rocks. Int. J. Rock Mech. Min. 138, 104598. https://doi.org/10.1016/j.ijrmms.2020.104598.

Li, J., Wu, K., 2022a. An efficient model for hydraulic fracture height growth considering the effect of bedding layers in unconventional shale formations. SPE J. 27 (6), 3740–3756. https://doi.org/10.2118/210572-PA.

Li, J., Wu, K., 2022b. Impact of horizontal weak interfaces on the hydraulic fracturing: from height growth to lateral propagation. In: SPE/AAPG/SEG Unconventional Resources Technology Conference. URTEC. 2022. https://doi.org/10.15530/urtec-2022-3723910. D021S032R003.

Liao, S., Hu, J., Zhang, Y., 2024. Mechanism of hydraulic fracture vertical propagation in deep shale formation based on elastic–plastic model. Eng. Fract. Mech. 295, 109806. https://doi.org/10.1016/j.engfracmech.2023.109806.

Liu, Y., Chen, C., Ma, T., et al., 2021. Experimental investigation on the initiation of hydraulic fractures from a simulated wellbore in laminated shale. Lithosphere-Us (Special 4). https://doi.org/10.2113/2021/4152918.

Lu, Q., Ei-Fayoumi, A., Adachi, J., et al., 2023. Laboratory demonstration of the impact of weak interfaces and layered rock properties on hydraulic fracture containment and height growth. Geomech. Geophys. Geo 9 (1), 113. https://doi.org/10.1007/s40948-023-00649-6.

Ma, J., Li, X., Yao, Q., et al., 2023. Numerical simulation of hydraulic fracture extension patterns at the interface of coal-measure composite rock mass with Cohesive Zone Model. J. Clean. Prod. 426, 139001. https://doi.org/10.1016/j.jclepro.2023.139001.

Miao, H., Guo, J.Y., Wang, Y.B., et al., 2023. Mineralogical and elemental geochemical characteristics of Taodonggou group mudstone in the Taibei Sag, Turpan–Hami Basin: Implication for its formation mechanism. Solid Earth 14 (9), 1031–1052. https://doi.org/10.5194/se-14-1031-2023, 2023.

Miao, H., Jiang, Z.X., Lu, J.M., et al., 2024. Hydrocarbon source and relationship between hydrocarbon charging process and reservoir tight period of the denglouku Formation tight sandstone gas reservoirs in the Xujiaweizi Fault Depression, songliao Basin. Nat. Resour. Res. 33, 1657–1684. https://doi.org/10.1007/s11053-024-10359-9.

Ouchi, H., Katiyar, A., Foster, J.T., et al., 2017. A peridynamics model for the propagation of hydraulic fractures in naturally fractured reservoirs. SPE J. 22 (4), 1082–1102. https://doi.org/10.2118/173361-PA.

Qin, M., Yang, D., 2023. Numerical investigation of hydraulic fracture height growth in layered rock based on peridynamics. Theor. Appl. Fract. Mech. 125, 103885. https://doi.org/10.1016/j.tafmec.2023.103885.

Sarmadi, N., Harrison, Nezhad, M.M., et al., 2024. Hydraulic fracture propagation in layered heterogeneous rocks with spatially Non-Gaussian random hydromechanical features. Rock Mech. Rock Eng. 57, 8117–8140. https://doi.org/10.1007/s00603-024-03954-y.

Shentu, J., Lin, B., Jin, Y., et al., 2024. Investigation of hydraulic fracture propagation in conglomerate rock using discrete element method and explainable machine learning framework. Acta Geotech. 19 (6), 3837–3862. https://doi.org/10.1007/s11440-024-02317-9.

Slatt, R.M., O'Brien, N.R., 2011. Pore types in the Barnett and Woodford gas shales: Contribution to understanding gas storage and migration pathways in fine-grained rocks. AAPG Bull. 95 (12), 2017–2030. https://doi.org/10.1306/03301110145.

Sun, H.Q., Lu, Z.Y., Liu, L., et al., 2025. Technology and understanding of post-fracturing coring in three-dimensional development zone of Fuling shale gas, Sichuan Basin, SW China. Petrol. Explor. Dev. 52 (3), 731–745. https://doi.org/10.1016/S1876-3804(25)60599-4.

Tan, P., Jin, Y., Han, K., et al., 2017. Analysis of hydraulic fracture initiation and vertical propagation behavior in laminated shale formation. Fuel 206, 482–493. https://doi.org/10.1016/j.fuel.2017.05.033.

Tan, P., Jin, Y., Hou, B., et al., 2018. Laboratory investigation of shale rock to identify fracture propagation in vertical direction to bedding. J. Geophys. Eng. 15 (3), 696–706. https://doi.org/10.1088/1742-2140/aaa5d6.

Wang, H., Chen, L., Qu, Z., et al., 2020. Modeling of multi-scale transport phenomena in shale gas production—A critical review. Appl. Energy 262, 114575. https://doi.org/10.1016/j.apenergy.2020.114575.

Warpinski, N.R., Teufel, L.W., 1987. Influence of geologic discontinuities on hydraulic fracture propagation (includes associated papers 17011 and 17074). J. Petrol. Technol. 39 (2), 209–220. https://doi.org/10.2118/13224-PA.

Wu, L., Hou, Z., Xie, Y., et al., 2023. Fracture initiation and propagation of supercritical carbon dioxide fracturing in calcite-rich shale: A coupled thermal-hydraulic-mechanical-chemical simulation. Int. J. Rock Mech. Min. 167, 105389. https://doi.org/10.1016/j.ijrmms.2023.105389.

Wu, S., Gao, K., Feng, Y., et al., 2022b. Influence of slip and permeability of bedding interface on hydraulic fracturing: A numerical study using combined finite-discrete element method. Comput. Geotech. 148, 104801. https://doi.org/10.1016/j.compgeo.2022.104801.

Wu, S., Gao, K., Wang, X., et al., 2022a. Investigating the propagation of multiple hydraulic fractures in shale oil rocks using acoustic emission. Rock Mech. Rock Eng. 55 (10), 6015–6032. https://doi.org/10.1007/s00603-022-02960-2.

Xu, D., Hu, W.R., Gao, W., et al., 2015. Effects of laminated structure on hydraulic fracture propagation in shale. Petrol. Explor. Dev. 42 (4), 573–579. https://doi.org/10.1016/S1876-3804(15)30052-5.

Yaghoubi, A., 2019. Hydraulic fracturing modeling using a discrete fracture network in the Barnett Shale. Petrol. Explor. Dev. 119, 98–108. https://doi.org/10.1016/j.ijrmms.2019.01.015.

Yin, P.F., Yang, S.Q., Gao, F., et al., 2023. Numerical investigation on hydraulic fracture propagation and multi-perforation fracturing for horizontal well in Longmaxi shale reservoir. Theor. Appl. Fract. Mech. 125, 103921. https://doi.org/10.1016/j.tafmec.2023.103921.

Zeng, Q., Bo, L., Li, Q., et al., 2023b. Numerical investigation of hydraulic fracture propagation interacting with bedding planes. Eng. Fract. Mech. 291, 109575. https://doi.org/10.1016/j.engfracmech.2023.109575.

Zeng, Q., Bo, L., Liu, W., et al., 2023a. An investigation of hydraulic fracture propagation in multi-layered formation via the phase field method. Comput. Geotech. 156, 105258. https://doi.org/10.1016/j.compgeo.2023.105258.

Zhang, B., Guo, T., Qu, Z., et al., 2023b. Numerical simulation of fracture propagation and production performance in a fractured geothermal reservoir using a 2D FEM-based THMD coupling model. Energy 273, 127175. https://doi.org/10.1016/j.energy.2023.127175.

Zhang, J., Li, Y., Pan, Y., et al., 2021. Experiments and analysis on the influence of multiple closed cemented natural fractures on hydraulic fracture propagation in a tight sandstone reservoir. Eng. Geol. 281, 105981. https://doi.org/10.1016/j.enggeo.2020.105981.

Zhang, J., Yu, Q., Li, Y., et al., 2023a. Hydraulic fracture vertical propagation mechanism in interlayered brittle shale formations: An experimental investigation. Rock Mech. Rock Eng. 56 (1), 199–220. https://doi.org/10.1007/s00603-022-03094-1.

Zhang, W., Qu, Z., Guo, T., et al., 2019. Study of the enhanced geothermal system (EGS) heat mining from variably fractured hot dry rock under thermal stress. Renew. Energy 143, 855–871. https://doi.org/10.1016/j.renene.2019.05.054.

Zhang, Y., Guo, T., Chen, M., et al., 2024. Numerical simulation study of fracture height growth considering the influence of bedding planes. Comput. Geotech. 168, 106144. https://doi.org/10.1016/j.compgeo.2024.106144.

Zhang, Y., Liu, Z., Han, B., et al., 2022. Numerical study of hydraulic fracture propagation in inherently laminated rocks accounting for bedding plane properties. J. Pet. Sci. Eng. 210, 109798. https://doi.org/10.1016/j.petrol.2021.109798.

Zhao, Y., Zhang, Y., Yang, H., et al., 2022. Experimental study on relationship between fracture propagation and pumping parameters under constant pressure injection conditions. Fuel 307, 121789. https://doi.org/10.1016/j.fuel.2021.121789.

Zheng, Y., He, R., Huang, L., et al., 2022. Exploring the effect of engineering parameters on the penetration of hydraulic fractures through bedding planes in different propagation regimes. Comput. Geotech. 146, 104736. https://doi.org/10.1016/j.compgeo.2022.104736.

Zhou, S., Zhuang, X., Rabczuk, T., 2018. A phase-field modeling approach of fracture propagation in poroelastic media. Eng. Geol. 240, 189–203. https://doi.org/10.1016/j.enggeo.2018.04.008.

Zhou, W., Shi, G., Wang, J., et al., 2022. The influence of bedding planes on tensile fracture propagation in shale and tight sandstone. Rock Mech. Rock Eng. 2022, 1–14. https://doi.org/10.1007/s00603-021-02742-2.

Zhou, Z., Jin, Y., Zeng, Y., et al., 2020a. Investigation on fracture creation in hot dry rock geothermal formations of China during hydraulic fracturing. Renew. Energy 153, 301–313. https://doi.org/10.1016/j.renene.2020.01.128.

Zhou, T., Wang, H.B., Li, F.X., et al., 2020b. Numerical simulation of hydraulic fracture propagation in laminated shale reservoirs. Petrol. Explor. Dev. 47 (5), 1117–1130. https://doi.org/10.1016/S1876-3804(20)60122-7.

Zhu, W.C., Tang, C.A., 2002. Numerical simulation on shear fracture process of concrete using mesoscopic mechanical model. Constr. Build. Mater. 16 (8), 453–463. https://doi.org/10.1016/S0950-0618(02)00096-X.

Zou, C.N., Zhu, R.K., Wu, S.T., et al., 2012. Types, characteristics, genesis and prospects of conventional and unconventional hydrocarbon accumulations: taking tight oil and tight gas in China as an instance. Acta Pet. Sin. 33 (2), 173.

Zou, J., Jiao, Y.Y., Tan, F., et al., 2021. Complex hydraulic-fracture-network propagation in a naturally fractured reservoir. Comput. Geotech. 135, 104165. https://doi.org/10.1016/j.compgeo.2021.104165.